

Large scale star formation in Auriga region

A. K. Pandey,^{1*} Saurabh Sharma,¹ N. Kobayashi,^{2,3}
Y. Sarugaku,³ and K. Ogura⁴

¹*Aryabhata Research Institute of Observational Sciences (ARIES), Manora Peak, Nainital, 263 002, India*

²*Institute of Astronomy, University of Tokyo, 2-21-1 Osawa, Mitaka, Tokyo 181-0015, Japan*

³*Kiso Observatory, School of Science, University of Tokyo, Mitake-mura, Kiso-gun, Nagano 397-0101, Japan*

⁴*Kokugakuin University, Higashi, Shibuya-ku, Tokyo 150-8440, Japan*

Accepted XXX. Received YYY; in original form ZZZ

ABSTRACT

New observations in the *VI* bands along with archival data from the 2MASS and *WISE* surveys have been used to generate a catalog of young stellar objects (YSOs) covering an area of about $6^\circ \times 6^\circ$ in the Auriga region centered at $l \sim 173^\circ$ and $b \sim 1^\circ.5$. The nature of the identified YSOs and their spatial distribution are used to study the star formation in the region. The distribution of YSOs along with that of the ionized and molecular gas reveals two ring-like structures stretching over an area of a few degrees each in extent. We name these structures as Auriga Bubbles 1 and 2. The center of the Bubbles appears to be above the Galactic mid-plane. The majority of Class I YSOs are associated with the Bubbles, whereas the relatively older population, i.e., Class II objects are rather randomly distributed. Using the minimum spanning tree analysis, we found 26 probable sub-clusters having 5 or more members. The sub-clusters are between ~ 0.5 pc - ~ 3 pc in size and are somewhat elongated. The star formation efficiency in most of the sub-cluster region varies between 5% - 20% indicating that the sub-clusters could be bound regions. The radii of these sub-clusters also support it.

Key words: stars: formation – stars: pre-main-sequence – (ISM:) H II regions

1 INTRODUCTION

Massive stars (mass $\gtrsim 8 M_\odot$, OB spectral types) are usually found in stellar groups, i.e., star clusters or OB associations. This is expected as a majority of the stars are born in groups embedded in molecular clouds (see e.g., Lada & Lada 2003). However, the recent study by Ward & Kruijssen (2018) favors the hierarchical star formation model, in which a minority of stars forms in bound clusters and large-scale, hierarchically-structured associations are formed in-situ. Recent mid-infrared (MIR) surveys have also shown that a significant number of young stellar objects (YSOs) form in the distributed mode (see e.g., Koenig et al. 2008; Panwar et al. 2019).

O stars are the major source of Lyman continuum (Lyc) ionizing radiation. Also strong stellar winds from O and B stars release kinematic energy of up to 10^{51} ergs over their lifetimes (McCray & Kafatos 1987). Since young star clusters/ OB associations have several OB stars (mass $\gtrsim 8 M_\odot$),

the ionizing radiation and stellar wind of these stars are the dominant input power source into the surroundings at the initial phase, creating a shell/ bubble of radius ≤ 100 pc at the end of the wind-driven phase (McCray & Kafatos 1987). These shells can be observed in H I 21 cm line observations, also they can be observable in X-ray from their hot interiors, in optical due to emission from ionized gas and in infrared (IR) from swept up dust in the shell (Oey et al. 2005; Cichowolski et al. 2014; Szegedi-Elek et al. 2019). Actually expanding shells of dense gas around H II regions have been found in several previous studies, e.g., around λ Orionis, Gemini OB1, W33, the Cepheus Bubble (cf. Patel et al. 1998, and reference therein). In the course of expansion of the shells the remaining molecular cloud could be induced to form a second generation of stars.

However the energy input by these massive stars to the surroundings toward the end phase is probably dominated by their supernova (SN) explosions, which could release energy of $\sim 10^{51}$ ergs; however, only a few cases are known which provide direct evidence of supernova-remnant (SNR)-molecular cloud interaction (McCray & Kafatos 1987;

* E-mail: pandey@aries.res.in

Patel et al. 1998; Churchwell et al. 2006). The expansion of the SN blast waves also could produce a new generation of stars. Only morphological signatures are often invoked to prove a physical association between SNRs and star-forming molecular clouds (e.g., Reynoso & Mangum 2001, and reference therein). The most convincing evidence is the line broadening due to shocked molecular gas (Frail & Mitchell 1998; Reach & Rho 1999).

Kang et al. (2012) made H I 21 cm line observations and detected high velocity H I gas at $l \sim 173^\circ$, $b \sim 1.5^\circ$. They suggested a large scale star formation activity possibly associated with an SN explosion in the H II complex G173+1.5. The low resolution H I survey reveals that this high velocity gas has velocities extended beyond those allowed by Galactic rotation. They designated this feature as Forbidden Velocity Wing 172.8+1.5, which is composed of knots, filaments, Sharpless H II regions distributed along a radio continuum loop of size $4^\circ.4 \times 3^\circ.4$. They concluded that the H I gas is well correlated with the radio continuum loop and both of them seem to trace an expanding shell. The expansion velocity and kinetic energy of the shell is estimated as 55 km s^{-1} and $2.5 \times 10^{50} \text{ erg}$, suggesting that it could be due to a SN explosion. The authors proposed that the progenitor may have belonged to a stellar association near the center of the shell, and this SN explosion triggered the formation of the H II regions.

The H II complex G173+1.5 associated with the Forbidden Velocity Wing features seems to be an excellent site to study SN-triggered star formation. A very general description of many star forming regions (SFRs) in Auriga is given in Reipurth & Yan (2008), and the individual regions have been discussed in several previous studies (e.g., Lafon et al. 1983; Heyer et al. 1996; Jose et al. 2008; Pandey et al. 2013; Mel'Nik & Dambis 2009; Marco & Negueruela 2016). By mapping the spatial distribution of YSOs around $l \sim 173^\circ$, $b \sim 1.5^\circ$, we can study the star formation in this whole region; it is, however, a challenging task to procure uniform optical data over such a large region ($\sim 4^\circ.4 \times 3^\circ.4$). The Kiso Wide field Camera (KWFC, Sako et al. 2012), mounted on the Kiso Schmidt telescope operated by the Institute of Astronomy of the University of Tokyo, Japan, covers a FOV of $2^\circ.2 \times 2^\circ.2$ and enables to provide homogeneous optical data for a very wide area such as the region of the H II complex G173+1.5. Thus by combining $V&I$ optical photometry obtained with this facility with archival data, we can analyze the distribution of the low-mass YSOs and gas/dust around $l \sim 173^\circ$ in Auriga, aiming to study the star formation in this region. We also attempt to understand the origin and evolution of the expanding H I shell. As a result, we have found two ring-like structures of YSOs/gas/dust distribution extending over an area of a few degrees. They are termed as Auriga Bubbles 1 and 2. In this paper, however, we deal mainly with the former, and Auriga Bubble 2 will be discussed in a forthcoming paper. Section 2 describes the observations, data reduction and completeness of the data. The YSO identification technique, the resulting YSOs sample and their physical parameters are derived in Section 3. In Section 4 we discuss the characteristics and distribution of identified YSOs, distribution of gas and dust as well as the star formation scenario in the region. We will conclude in Section 5.

2 OBSERVATIONS AND DATA REDUCTION

2.1 Kiso Observations

Optical ($V&I$) data for nine overlapping regions of Auriga (Auriga 1 - Auriga 9, cf. Fig. 1) were procured with KWFC (FOV $\sim 2.2^\circ \times 2.2^\circ$; scale 0.946 arcsec/pixel; Sako et al. 2012) on the 1.05-m Schmidt telescope at Kiso Observatory, Japan during the nights of 06, 07 December 2012 and 27 December 2014. KWFC, an optical wide-field 64 megapixel imager with 4 SITE and 4 MIT Lincoln Laboratory (MIT/LL) $15\mu\text{m}$ 2K×4K CCDs is attached to the prime focus of the Kiso Schmidt telescope. The details of the instrument can be found in Sako et al. (2012) and Morokuma et al. (2014). The observations were carried out in the unbinned and slow readout mode. In this mode, the readout noise is about 20 and 5-10 electrons for the SITE and MIT/LL CCDs, respectively. A number of short and deep exposures were taken. The detailed log of the observations is given in Table 1. Several bias and dome-flat frames were also taken each night.

Initial processing (bias subtraction, flat-fielding and cosmic ray correction) of the data frames was done by using the IRAF¹ data reduction package. Astrometric calibration and image co-addition were carried out by using the SCAMP² and SWarp³ software, respectively. The total FOV observed in this study is $\sim 6^\circ \times 6^\circ$ and is shown in Fig. 1. Photometry of the cleaned frames was carried out by using DAOPHOT-II software which includes FIND, PHOT, PSF and ALLSTAR sub-routines (Stetson 1987, 1994). The point spread function (PSF) was obtained for each frame by using several uncontaminated stars. When brighter stars were saturated on deep exposure frames, their magnitudes have been taken from short exposure frames. We used the DAOGROW program for construction of an aperture growth curve required for determining the difference between the aperture and PSF magnitudes.

To calibrate the data we used the following procedure. We first calibrated the data for the Auriga 1 field (see Fig. 1) using the photometric data of NGC 1960 taken from Sharma et al. (2006) which provides photometry in the U, B, V, R and I bands down to a limiting magnitude of $V=20 \text{ mag}$ (error $< 0.1 \text{ mag}$) in a FOV of $\sim 1^\circ \times 1^\circ$. This cluster lies in the Auriga 1 field. The area covering the observations of NGC 1960 is also shown in Fig. 1.

After calibrating the Auriga 1 field, stars lying in the common overlapping area of Auriga 1 and Auriga 2 were taken as the secondary standards to calibrate the Auriga 2 field. The common stars of Auriga 2 and Auriga 4 were taken as the secondary standards to calibrate the Auriga 4 field and so on. To translate the instrumental magnitudes to the standard magnitudes the following calibration equations, derived by using a least-square linear regression, were used:

$$V - v = M1 \times (V - I) + C1 \quad (1)$$

$$(V - I) = M2 \times (v - i) + C2, \quad (2)$$

¹ IRAF is distributed by National Optical Astronomy Observatories, USA

² <http://www.astromatic.net/software/scamp>

³ <http://www.astromatic.net/software/swarp>

where V and $(V - I)$ are the standard magnitudes and colours from Sharma et al. (2006), respectively; v , and $(v - i)$ are the instrumental magnitudes and colours, respectively; C1, C2 and M1, M2 are the zero-point constants and colour coefficients, respectively. Fig. 2 plots, as an example, the $(V - I)$ vs. $(V - v)$ and $(v - i)$ vs. $(V - I)$ diagram for the stars in NGC 1960. Fig. 3 (top panels) plot the difference between the NGC 1960 data from Sharma et al. (2006) and the calibrated V magnitudes and $(V - I)$ colours of the NGC 1960 region obtained by using the equations 1 and 2. The standard deviation in ΔV and $\Delta(V - I)$, in the magnitude range $V \sim 13.5 - 19.0$ mag, is 0.09 and 0.08 mag, respectively. The values of all the zero-point constants and colour coefficients for various fields (Auriga 1 - Auriga 9) are given in Table 2.

The Auriga 3 field was calibrated by using the common stars in Auriga 5 and Auriga 3 as secondary standards as described earlier in this section. We further used the common stars lying in Auriga 1 and Auriga 3 to get another set of the transformed standard magnitudes for Auriga 1 stars. Fig. 3 (middle panel) and Table 3 shows the residuals Δ , between the two sets of calibrated data of Auriga 1 in V magnitudes and $(V - I)$ colours. The standard deviation in ΔV and $\Delta(V - I)$, in the magnitude range $V \sim 13.5 - 19.0$ mag is ~ 0.02 and ~ 0.03 mag, respectively. Although there is some trend in lower panel, but the scatter is small. The comparison of these two transformed standard data indicates a fair agreement. Here we would like to point out that although the uncertainty due to the calibration shown in Fig. 2 is not negligible, the uncertainty in optical data due to calibration are not crucial for the scientific results of the present study as they can be safely assumed to be negligible compared to those associated with the analysis of the Spectral Energy Distribution (SED) aimed at the derivation of stellar and disk parameters (cf. Section 3.3.1). To ensure the quality of the calibration of the data we further calibrated the Auriga 3 field using the NGC 1960 data from Sharma et al. (2006) and compared the calibrated photometric data of common stars in the FOVs of Auriga 1 and Auriga 3. The comparison is shown in the lower panel of Fig. 3. Table 4 shows residuals between the two photometric calibrations. The standard deviation in ΔV and $\Delta(V - I)$, in the magnitude range $V \sim 13.5 - 19.0$ mag is ~ 0.07 and ~ 0.08 mag, respectively. The comparison of these two independently calibrated data indicates a fair agreement and ensures the reliability of the calibration. The typical DAOPHOT errors in magnitude as a function of the corresponding magnitudes are shown in Fig. 4. It can be seen that the errors become large (~ 0.1 mag) for stars $V \sim 20$ mag. More than 0.47 million stars have errors less than 0.1 mag in V and I bands and these stars have been used for analysis in the ensuing sections.

2.2 Archival data: 2MASS and WISE data

To investigate the star formation in the Auriga Bubble region we also used near/mid infra-red (NIR/MIR) data from the Two Micron All Sky Survey (2MASS, Cutri et al. 2003) and the Wide-field Infrared Survey Explorer survey (WISE, Wright et al. 2010) archived data in addition to the optical VI data from the Kiso Schmidt telescope.

WISE is a 40-cm telescope in low-Earth orbit that surveyed the whole sky in four mid-IR bands at 3.4, 4.6, 12, and

22 μm (bands $W1$, $W2$, $W3$, and $W4$) with nominal angular resolutions of $6''.1$, $6''.4$, $6''.5$, and $12''.0$ in the respective bands (Wright et al. 2010). In this paper, we make use of the AllWISE source catalog, which provides accurate positions, apparent motion measurements, four-band fluxes and flux variability statistics for over 747 million objects. The online explanatory supplement⁴ and Marsh & Jarrett (2012) describe the WISE source detection method in detail. The AllWISE catalog is searchable via NASA/IPAC Infrared Science Archive (IRSA). It also provides information on 2MASS counterparts.

We have also used the 2MASS Point Source Catalog (PSC, Cutri et al. 2003) for near-IR (NIR) JHK_s photometry of all the sources (including those sources which do not have WISE photometry) in the Auriga Bubble region. This catalog is reported to be 99% complete down to the limiting magnitudes of 15.8, 15.1 and 14.3 in the J , H and K_s band, respectively⁵.

2.3 Completeness of the data

To have an unbiased study of star formation in the region, it is vital to know the completeness of the data in terms of magnitudes/ masses for the sample YSOs identified. The photometric data may be incomplete due to various reasons, e.g., nebulosities, crowding of stars, detection limit etc (Sagar & Richtler 1991; Sharma et al. 2008).

To check the completeness factor for the optical data we used the ADDSTAR routine of DAOPHOT II. This method has been used by various authors (cf. Sharma et al. 2007, 2008, and references therein). Briefly, the method consists of randomly adding artificial stars of known magnitudes and positions into the original frame. The frames are reduced by using the same procedure used for the original frame. The ratio of the number of stars recovered to those added in each magnitude interval gives the completeness factor as a function of magnitude. The luminosity distribution of artificial stars is chosen in such a way that more stars are inserted into the fainter magnitude bins. In all about 15% of the total stars are added so that the crowding characteristics of the original frame do not change significantly (see Sagar & Richtler 1991). We found that the present optical data for I band are complete at $\sim 90\%$ level for 17.75 magnitude (cf. Fig. 5).

The estimate of the completeness of the present YSO sample is rather difficult as it is limited by several factors. For example, the bright nebulosity in the WISE bands significantly limits the point source detection. The YSO identification on the basis of 2MASS - WISE colours may be limited by the sensitivity of the 2MASS survey and saturation of $W3$ and $W4$ images. Variable reddening and stellar crowding characteristics across the region could also affect the local completeness limit. The completeness of the YSO selection using the NIR data is also dictated by the amount of IR excess, the evolutionary status of disks etc. In the present study the larger WISE PSF may also hamper the detection of YSOs in the crowded region. All these effects are difficult to quantify.

⁴ <http://wise2.ipac.caltech.edu/docs/release/allwise/expsup/>

⁵ <http://tdc-www.harvard.edu/catalogs/tmpsc.html>

3 RESULTS

3.1 YSO identification

In the present study the 2MASS data along with the *WISE* data have been used to identify and classify the YSOs associated with the Auriga Bubbles 1 and 2 using the following classification schemes. YSOs are generally classified as Class 0, Class I, Class II or Class III sources on the basis of the infrared slopes of their spectral energy distributions (Barsony 1994; Lada et al. 2006). YSOs of the early stages (i.e., Class 0 and I) are usually deeply buried inside the molecular clouds, hence detection of them at optical wavelengths is difficult. The most prominent feature of these YSOs is accreting circumstellar disks and envelopes. The radiation from the central YSO is absorbed by the circumstellar material and re-emitted in NIR/MIR. Therefore, Class I (and Class II as well) sources can be probed through their IR excess (compared to normal stellar photospheres).

3.1.1 *WISE* classification

The four wave-bands of *WISE* are useful to detect mid-IR emission from cold circumstellar disk/envelope material in YSOs. This makes *WISE* all-sky survey as a readily available tool to identify and classify YSOs, in a similar way to what can be done with *Spitzer* (Allen et al. 2004; Gutermuth et al. 2008, 2009, and others) but over the entire sky. We use the AllWISE Source Catalog to search for YSOs adopting the criteria given by Koenig & Leisawitz (2014). We refer Figure 3 of Koenig & Leisawitz (2014) to summarize the entire scheme. This method includes the selection of candidate contaminants (AGN, AGB stars and star forming galaxies). Out of 40788 *WISE* source meeting photometric quality flags, 22238 sources were excluded from the data file as contaminants on the basis of selection criteria of Koenig & Leisawitz (2014). In the present study we followed and applied the photometric quality criteria for different *WISE* bands as given in Koenig & Leisawitz (2014).

3.1.1.1 *WISE* three-band classification We applied this classification scheme to all the sources that were detected in three *WISE* bands (namely *W1*, *W2* and *W3*) and satisfying the photometric quality criteria as given in Koenig & Leisawitz (2014). The YSOs were selected on the basis of their (*W1* – *W2*) and (*W2* – *W3*) colours according to the criteria given by (Koenig & Leisawitz 2014), which are based on the colours of known YSOs in Taurus, extragalactic sources, and Galactic contaminants. This approach efficiently separates out IR excess contaminants such as star forming galaxies, broad-line active galactic nuclei, unresolved shock emission knots, objects that suffer from polycyclic aromatic hydrocarbon (PAH) emissions etc. (see e.g., figure 2 of Fischer et al. 2016). Fig. 6 (top left-hand panel) shows the (*W2* – *W3*) versus (*W1* – *W2*) *WISE* two-colour diagram (TCD) for all the sources in the region, where candidate YSOs classified as Class I and Class II are shown by red stars and red squares, respectively. However, it is worthwhile to mention that there could be a overlap between Class I and Class II objects as can be seen in figure 5 of Koenig & Leisawitz (2014). However, this is not expected to affect our discussion on bubbles as we are using both

Class I and Class II YSOs having age ≤ 1 Myr to delineate the structure of the bubbles (cf. Section 4.3, Fig. 18).

3.1.1.2 *WISE* four-band classification *W4* photometry has been used to identify candidates transition disk objects and also to retrieve candidate protostars which might have been classified as AGN candidate on the basis of the *WISE* three band classification scheme (cf. Sec. 3.1.1.1). Fig. 6 (top right-hand panel) shows the (*W3* – *W4*) versus (*W1* – *W2*) TCD for all the sources in the region, where probable YSOs classified as transition disk sources and protostars are shown by red pentagons and red circles, respectively. The classification discussed in this section yields one and four transition disk source and protostars, respectively.

3.1.1.3 2MASS and *WISE* classification Since the studied region has highly variable nebulosity, many sources in the region may not be detected at longer wavelengths due to the saturation of detectors, hence the selection of YSOs on the basis of only *WISE* bands photometry may not be complete. Therefore, we use 2MASS *H*, *K_s* data along with *W1* and *W2* band *WISE* data as some sources might have not been detected in the *W3* band, but have possibility of detection in the 2MASS *H* and *K* band (Koenig & Leisawitz 2014). Fig. 6 (bottom left-hand panel) shows the (*W1* – *W2*) versus (*H* – *K*) TCD for all the sources in the region, where probable YSOs classified as Class I and Class II are shown by red stars and red squares, respectively. All the YSOs identified above have been checked against the possibility of being AGB stars as discussed by Koenig & Leisawitz (2014). Finally on the basis of the *WISE* data we classified 154 and 331 sources as probable Class I and Class II YSOs.

3.1.2 2MASS classification

The (*J* – *H*)/(*H* – *K*) NIR TCD is also a useful tool to identify pre-main sequence (PMS) objects. It is possible that some of the candidate YSOs might have not been detected on the basis of *WISE* data, hence we have also used 2MASS *JHK* three band data to identify additional YSOs. Fig. 6 (bottom right-hand panel) displays the NIR TCD for all the stars which have not been detected in the *WISE* survey or do not meet the photometric quality criterion (cf. Section 3.1.1) in the region studied. The 2MASS magnitudes and colours have been converted into the California Institute of Technology (CIT) system⁶. The solid and long dashed lines in Fig. 6 (bottom left-hand panel) represent unreddened main sequence (MS) and giant branch loci (Bessell & Brett 1988), respectively. The dotted line indicates the intrinsic loci of CTTSs (Meyer et al. 1997). The parallel dashed lines are the reddening vectors drawn from the tip (spectral type M4) of the giant branch (‘left reddening line’), from the base (spectral type A0) of the MS branch (‘middle reddening line’) and from the tip of the intrinsic CTTSs line (‘right reddening line’). The extinction ratios $A_J/A_V = 0.265$, $A_H/A_V = 0.155$ and $A_K/A_V = 0.090$ have been adopted from Cohen et al. (1981). The sources lying in the ‘F’ region could be either field stars (MS stars, giants), Class III or Class II sources with small NIR excesses. The

⁶ <http://www.astro.caltech.edu/~jmc/2mass/v3/transformations/>

sources lying in the ‘T’ region are considered to be mostly classical T-Tauri stars (CTTSs, i.e., Class II objects). The sources lying in the ‘P’ region - redward of the right redening line - are most likely Class I objects (protostellar-like objects; Ojha et al. 2004b). In this scheme we consider only those sources as YSOs that lie at a location above the intrinsic loci of CTTSs with margins larger than the errors in their colours. This classification criterion yields 21 and 204 probable Class I and Class II YSOs, respectively.

3.2 YSO sample

On the basis of the criteria discussed above we have compiled a catalog of 710 YSOs in an area of $\sim 6 \times 6$ degree², divided into 175 Class I and 535 Class II YSOs. A portion of the catalog is shown in Table 5, which lists the positions of YSOs, their magnitudes at various bands, and classification. The complete catalog is available in an electronic form only. The optical magnitudes of the nearest optical counterparts for 176 YSOs which have been found within a match radius of 2 arcsec are also given in Table 5. Here, it is worthwhile to mention that no multiple identification between the optical and IR counterparts of YSOs are found within 2 arcsec.

As assumed in various previous studies, the peak of the observed luminosity function can be considered as the 90% completeness limit of the data (cf. Evans et al. 2003; Willis et al. 2013; Jose et al. 2013, 2016; Sharma et al. 2016). We constructed the luminosity function for each band (see Fig. 7). The resultant completeness limits of the optical and *WISE* data are given in Table 6. The completeness limit in the *I* band obtained here agrees well with that obtained in Sec 2.3. As mentioned in Sec 2.2, we assume that the 2MASS *JHK* data have completeness of $\sim 90\%$ at the limiting magnitudes of 15.8, 15.1 and 14.3 for the *J*, *H* and *K* bands respectively.

3.2.1 Unidentified Class III (diskless) sources

In the present study we have not attempted to identify diskless YSOs. The Class III sources may possibly have a different spatial distribution in the Auriga region as compared to the Class I and II YSOs and inclusion of these sources may have impact on the parameters described in the ensuing sections. It is worthwhile to mention that disk fraction estimates in young clusters having age ≤ 3 Myr varies from 60-70% ($M \lesssim 2 M_{\odot}$) and 35 - 40% ($M > 2 M_{\odot}$) (Ribas et al. 2015), whereas the disk half-life estimates varies from 1.3 Myr to 3.5 Myr (Richert et al. 2018, and references therein). Since the missing YSO mass due to the incompleteness of our YSO search criteria as well as to unidentified Class III sources may play a role in the analysis to be carried out in the ensuing sections, we will assume that 50% of the total YSO population is missed in the present YSO sample.

3.3 Physical properties of the identified YSOs

3.3.1 Spectral energy distribution

The YSOs can also be characterized from their SED. The SED fitting provides evolutionary stages and physical parameters such as mass, age, disk mass, disk accretion rate and photospheric temperature of YSOs and hence is an

ideal tool to study their evolutionary status. We constructed the SEDs of the YSOs using the grid models and Python version of SED fitting tools⁷ of Robitaille et al. (2006, 2007)⁸. The models were computed by using a Monte-Carlo based 20000 2-D radiation transfer calculations from Whitney et al. (2003a,b, 2004) and by adopting several combinations of a central star, a disk, an infalling envelope, and a bipolar cavity in a reasonably large parameter space and with 10 viewing angles (inclinations).

The SEDs were constructed by using the multiwavelength data (i.e. optical to MIR) with the condition that a minimum of 5 data points should be available. While fitting the models to the data we assumed the extinction and the distance as free parameters. Considering the errors associated with the distance estimates available in the literature, the range in distance estimate was assumed to vary between 2.0 kpc to 2.4 kpc. Since the extinction in the region is variable (cf. Jose et al. 2008; Pandey et al. 2013), we used a range for A_V of 1.6 to 30 mag. We further set photometric uncertainties of 10% for optical and 20% for both NIR and MIR. These values are adopted instead of the formal errors in the catalog in order to fit without any possible bias in underestimating the flux uncertainties. In Fig. 8, we show example SEDs of Class I and Class II sources, where the solid black curves represent the best-fit and the gray curves are the subsequent well-fits satisfying our requirements for good fit discussed below.

Since the SED models are highly degenerate, the best-fit model is unlikely to give an unique solution and the estimated physical parameters of the YSOs tabulated in Table 7 are the weighted mean with standard deviation of the physical parameters obtained from the models that satisfy $\chi^2 - \chi^2_{min} \leq 2N_{data}$, where χ^2_{min} is the goodness-of-fit parameter for the best-fit model and N_{data} is the number of input data points.

4 DISCUSSION

4.1 Physical conditions in the Auriga region

In this Section, we present a brief description of the identified YSOs, ionized gas and molecular clouds, along with their correlation with each other. The region contains five Sharpless H II regions Sh2-231 to Sh2-235. In addition it is reported that there are about 14 embedded SFRs having ages ~ 3 -5 Myrs (cf. Kang et al. 2012, and references therein). It has also been proposed that the formation of these young objects could have been triggered by a older generation of stars (Kang et al. 2012, and references therein).

4.1.1 Characteristics of the identified YSOs in the Auriga region

We have identified 710 YSOs in the Auriga Bubble region (cf. Table 5) and derived the physical parameters of 489 YSOs from the SED fitting analysis (cf. Table 7). These parameters were used in further analysis. Histograms of the age and

⁷ <https://sedfitter.readthedocs.io/en/stable/>

⁸ WISE fluxes were acquired from Dr. Thomas Robitaille through private communication

mass of these YSOs are shown in Fig. 9. The distribution of the ages estimated on the basis of SEDs indicates that $\sim 76\%$ (370/489) of the sources have ages ≤ 3.5 Myr. The masses of the YSOs are found to range between 0.75 to $9 M_{\odot}$, and a majority ($\sim 86\%$) of them are in the range of 1.0 to $3.5 M_{\odot}$. The A_V distribution shows a long tail indicating its large spread from $A_V=1$ - 27 mag, which is consistent with the nebulous nature of this region. The average age, mass and extinction (A_V) for this sample of YSOs are 2.5 ± 1.7 Myr, $2.4 \pm 1.1 M_{\odot}$ and 7.1 ± 4.1 mag, respectively.

The evolutionary classes of the identified 710 YSOs given in the Table 5 reveal that $\sim 25\%$ (175 out of 710) sources are Class I YSOs. The comparatively high percentage of Class I YSOs indicates the youth of this region.

4.1.2 The distribution of gas, dust and YSOs

Details on the environment and distribution of YSOs can be used to probe the star formation scenario in the region. In Fig. 10 (top left-hand panel), the H I contours by Furst et al. (1990) (black contours) and the ^{12}CO contour map (cyan contours) from Dame et al. (2001) along with the distribution of the YSOs are overlaid on the *WISE* $12 \mu\text{m}$ image. The *WISE* $12 \mu\text{m}$ image covers the prominent PAH features at $11.3 \mu\text{m}$, which is indicative of star formation activity (see e.g. Peeters et al. 2004). This figure reveals that ionized as well as molecular gas distribution is well correlated with that of YSOs. The distribution of ionized gas, molecular gas and YSOs indicates a ring-like structure spread over an area of a few degrees. The distribution of YSOs also reveals that a majority of Class I sources belong generally to this ring-like structure, whereas the comparatively older population, i.e. Class II objects, are rather randomly distributed throughout the region. As stated already we term this structure as Auriga Bubble1. Furthermore there is another, very well defined distribution of Class I and Class II objects towards the north-west of the H II complex G173+1.5, forming another bubble feature, which we call as Auriga Bubble2. Its nature will be discussed in an ensuing study.

4.1.3 Extinction and YSOs surface density maps

To quantify the extinction in the region and to characterize the structure of the molecular gas associated with various SFRs in the Auriga Bubble, we derived A_K extinction maps using the $(H - K)$ colours of field stars (cf. Gutermuth et al. 2011). To produce the extinction map we excluded the candidate YSOs (cf. Section 3.2) and probable contaminating sources (AGNs, AGB stars and star forming galaxies) using the procedure by Koenig & Leisawitz (2014) from the sample stars. Similar approaches were used by other studies also (e.g., Allen et al. 2008; Gutermuth et al. 2009; Jose et al. 2013, 2016; Sharma et al. 2016, and references therein). Mean values of A_K were derived by using the nearest neighbor (NN) method as described in detail by Gutermuth et al. (2005) and Gutermuth et al. (2009). Briefly, the mean value of $(H - K)$ colours of five nearest stars at each position in a grid of 30 arcsec was calculated for the entire Auriga region ($\sim 6^\circ \times 6^\circ$). The sources deviating above 3σ were excluded to calculate the final mean colours of each grid. The reddening law $A_K = 1.82 \times ((H - K)_{obs} - (H - K)_{int})$

by Flaherty et al. (2007) was used to convert the $(H - K)$ colours into A_K , where $(H - K)_{int} = 0.2$ was assumed as an average intrinsic colours of the field stars (see. Allen et al. 2008; Gutermuth et al. 2009). To eliminate the foreground contribution in generating the extinction map we used only those stars which have $A_K > 0.15 \times D$, where D is the distance in kpc (Indebetouw et al. 2005). The extinction map is sensitive down to $A_K \sim 2.8$ mag ($= A_V \sim 30$ mag). However, the derived A_K values are to be considered as lower limits, because the sources in the region with higher extinction might have not been detected in the present sample. The extinction map, smoothed to a resolution of 18 arcmin, is shown in blue colour in Fig. 10 (top right-hand panel). It is interesting to note that the extinction map resembles the general distribution of the molecular gas as outlined by the ^{12}CO emission map shown in Fig. 10 (top left-hand panel). It shows a concentration of molecular clouds towards Sh2 - 231 - 235. A comparison of the stellar density distribution and the morphology of the molecular material can provide a clue to the history of star formation in the region. The surface density maps of YSOs were generated by using the NN method as described by Gutermuth et al. (2005). We used the radial distance that contains 5 nearest YSOs to compute the local surface density in a grid size of 30 arcsec. The grid size identical to that of the extinction map was used to compare the stellar density and the gas column density. The density distribution of YSOs is shown in red colour in Fig. 10 (top right-hand panel). The distribution of the YSOs and molecular material shows a nice correspondence. Gutermuth et al. (2011) also found similar trends in eight nearby molecular clouds. Gutermuth et al. (2008) have shown that the sources in each of the Class I and Class II evolutionary stages have very different spatial distributions relative to that of the dense gas in their natal cloud. We have also compared the extinction map with the positions of YSOs of different evolutionary stages and found that the Class I sources are located towards the places with higher extinction. These properties agree well with previous findings in several star-forming regions such as W5 (Koenig et al. 2008; Deharveng et al. 2012), i.e., younger Class I sources are more clustered and closely associated with the densest molecular clouds in which they were born presumably, while the Class II sources are scattered probably by drifting away from their birthplaces.

4.2 Clustered population in the Auriga Bubble

4.2.1 Extraction of sub-clusters and the distribution of scattered YSO population

Many ground-based NIR surveys of molecular clouds (e.g., Lada et al. 1991; Strom et al. 1993; Carpenter et al. 2000; Porras et al. 2003; Lada & Lada 2003) have shown that molecular clouds host both dense ‘clustered’ and diffuse ‘distributed’ population. As discussed earlier the Auriga Bubble region contains several star forming subregions, hence a clustered distribution of YSOs is expected. Gutermuth et al. (2009) have used an empirical method based on the minimum spanning tree (MST) technique to isolate groupings (sub-clusters) from the more diffuse distribution of YSOs in nebulous regions. This method effectively isolates sub-structures without any type of smoothing (see e.g.,

Cartwright & Whitworth 2004; Schmeja & Klessen 2006; Bastian et al. 2007, 2009; Gutermuth et al. 2009). The sub-groups detected in this way have no biases regarding the shapes of the distribution and preserve the underlying geometry of the distribution (Gutermuth et al. 2009). In Fig. 10 (bottom left-hand panel) we plot the derived MSTs for the YSOs in the region. In order to isolate the sub-structures, we adopted a surface density threshold expressed by a critical branch length. With the help of an adopted MST branch length threshold we can identify local surface density enhancements. To do that, we used a similar approach to that suggested by Gutermuth et al. (2009). In Fig. 11, we plot the cumulative distribution for MST branch lengths, which shows a three-segment curve; a steep segment at short lengths, a transition segment at the intermediate lengths, and a shallow-sloped segment at long lengths. The majority of the sources are found in the steep segment, where the lengths are small (i.e., sub-cluster). Therefore, to isolate sub-cluster regions in the Auriga Bubble, we fitted two straight lines to the shallow and steep segments of the cumulative distribution function (CDF) and extended them to connect together. The intersection is adopted as the MST critical branch length, as shown in Fig. 11 (see also, Gutermuth et al. 2009). The sub-clusters of the SFRs were then isolated from the lower density distribution by clipping the MST branches longer than the critical length described above. Similarly, we defined the extended area for the SFR by selecting the point where the curved transition segment meets the shallow-sloped segment at longer spacings. This range represents the extended region of star formation or the area where YSOs might have moved away from the sub-clusters due to dynamical evolution, and we have named this region as the active region. The black dots connected with black lines and the blue dots connected with blue lines in Fig. 10 (bottom left-hand panel) are the branches smaller than the critical length for the sub-clusters and the active region, respectively. We have also plotted the convex hulls (cf. Gutermuth et al. 2009) for the active region in Fig. 10 (bottom left-hand panel) with solid purple lines. The physical details of the sub-groups (sub-clusters) and the active regions are given in Tables 8, 9 and 10. In total, we have identified 9 active regions and 26 probable sub-clusters having at-least 5 YSO members in the Auriga Bubble region. Although sub-clusters with a small number of members have been reported in previous studies, e.g., Gutermuth et al. (2009, N=10), Cartwright & Whitworth (2004, N=7-10) and Sharma et al. (2016, N=10), however it is worthwhile to mention that smaller numbers of YSOs in some of the probable sub-clusters may introduce relatively large errors in the derived physical parameters discussed in the ensuing subsections. The median value of the critical branch lengths for the sub-clusters and the active regions are 2 pc and 9 pc, respectively. In Fig. 10 (bottom right-hand panel) we can see a correlation between the identified active regions with the extinction contours and the YSO locations in the Auriga Bubble.

In many SFRs YSOs are observed to have both diffuse and clustered spatial distribution. For example, Koenig et al. (2008) have analyzed the clustering properties across the W5 region and found 40-70% of the YSOs belong to groups with ≥ 10 members and the remaining were described as scattered populations. Using the All-

WISE database, Fischer et al. (2016) identified 479 YSOs in a 10×10 degree² region centered on the Canis Major star-forming region. Their YSO sample contains 144 and 335 Class I and Class II YSOs, respectively. On the basis of the MST of the YSO distribution, Fischer et al. (2016) concluded that there were 16 groups with more than four members. Of the 479 YSOs, 53% are in such groups. Gutermuth et al. (2009) presented a uniform MIR imaging and photometric survey of 36 nearby young clusters and groups using Spitzer IRAC and MIPS. They found 39 clusters/sub-clusters with 10 or more YSO members. Of the 2548 YSOs identified, 1573 (62%) are members of one of these clusters/sub-clusters. Although the sub-clusters in the Auriga Bubble region have sizes of the order of a few parsecs, however, some of the member stars might have moved away in the last few Myr due to dynamical and environmental effects (Miao et al. 2006). Weidner et al. (2011) used N-body calculations to study the numbers and properties of escaping stars from young embedded star clusters during the first 5 Myr of their existence prior to the removal of gas from the system. They found that these clusters can lose substantial amounts (up to 20%) of stars within 5 Myr. In the present sample, the YSOs formed in the sub-clusters having a mean velocity of ~ 2 km s⁻¹ (cf. Weidner et al. 2011) can travel a distance of ~ 2 -6 pc in 1-3 Myr of their formation. Therefore, we expect that the effect of escaping members from the sub-clusters/active regions must be insignificant. We have estimated that the fraction of the scattered YSO population (the YSOs outside sub-clusters, but in the active regions) is about $\sim 37\%$ of the total YSOs in the whole active regions. Similar numbers ($\sim 40\%$) in the case of 8 bright rimmed clouds (Sharma et al. 2016) and 5 embedded clusters (Chavarría et al. 2014) have also been reported in previous studies. The explanation for the scattered populations may include: escape of sub-clusters/cluster members due to their dynamical interaction and isolated star formation (for details, Elmegreen & Efremov 1997; Lada & Lada 2003; Koenig et al. 2008; Evans et al. 2009; Elmegreen et al. 2014; Chavarría et al. 2014; Panwar et al. 2019).

4.2.2 Sub-cluster morphology and structural parameters

Known SFRs show a wide range of sizes, morphologies and star numbers (cf. Gutermuth et al. 2008, 2009, 2011; Chavarría et al. 2014). We use cluster's convex hull radii (R_H) and aspect ratios to investigate their morphology (see Table 9 and Fig. 12). Here we would like to point out that the present procedure is applied to the sample which contains only Class I and Class II YSOs and does not include Class III YSOs. The similar approach has been adopted in previous studies also (Gutermuth et al. 2009; Sharma et al. 2016). However, as discussed in Section 3.2.1, the contribution of diskless YSOs (i.e. Class III sources) in star-forming regions having age 2-3 Myr may be about 50% of the total YSO population. This missing population may play a significant role in estimating various parameters discussed in the ensuing sections. Hence we also estimate parameters by assuming the contribution of Class III sources as 50% of the total YSO population.

A majority of the sub-clusters identified in the present sample show an elongated morphology with the median value of the aspect ratios around 1.6. The median number of

YSOs in the sub-clusters and the active regions are 9 and 38, respectively (cf. Table 10). The median MST branch length for these sub-clusters is found to be ~ 0.5 pc. The total sum of YSOs in the active regions is 546, out of which 345 (63%) falls in the sub-clusters. The YSOs in the Auriga Bubble have mean surface densities mostly between 0.3 and 7.5 pc^{-2} (see Table 8 and Fig. 13). The median values for the surface densities for the sub-clusters and the active region come out to be around 1.35 pc^{-2} and 0.1 pc^{-2} , respectively. The peak surface densities vary between $\sim 0.5 - 18 \text{ pc}^{-2}$ with a median value of 4 pc^{-2} for our sample (cf. Table 8 and Fig. 13). As in the case of low-mass embedded clusters studied by Chavarría et al. (2014), we found a weak proportionality between the peak surface density and the number of cluster members, suggesting that the clusters are better characterized by their peak YSO surface density.

The spatial distribution of YSOs in a SFR can be investigated with the help of the structural Q parameter (Cartwright & Whitworth 2004; Schmeja & Klessen 2006). It is used to measure the level of hierarchical versus radial distributions of a set of points, and it is defined by the ratio of the MST-normalized mean branch length to the normalized mean separation between points (cf. Chavarría et al. 2014, for details). If the normal values are used, the Q parameter becomes independent on the cluster size (Schmeja & Klessen 2006). A group of points distributed radially will have a high Q value ($Q > 0.8$), while clusters with a more fractal distribution will have a low Q value ($Q < 0.8$) (Cartwright & Whitworth 2004). We find that the groups of the YSOs in the present study (including only Class I and II sources) have median Q values less than 0.8 (0.71 in sub-clusters and 0.52 in active regions, cf. Tables 9 and 10), indicating a more fractal distribution. Chavarría et al. (2014) have found a weak trend in the distribution of Q values per number of members, suggesting a higher occurrence of sub-clusters merging in the most massive cluster, which reduces the Q value. A similar trend can be noticed in Fig. 14 (left-hand panel).

4.2.3 Associated molecular material, stellar mass and Jeans length

The mean A_K values for the identified sub-clusters have been found in the range of 0.6 and 1.3 mag, with a median value of 0.9 mag (cf. Table 10 and Fig. 15). A weak correlation (Spearman's correlation coefficient 'r' = 0.6 with 95% confidence interval of 0.3 to 0.8) between the peak A_K and the number of cluster members can be noticed in Fig. 15. The median A_K value for the active regions is 0.6 mag, which is lower than the sub-cluster value, naturally indicating the YSO distribution of higher density towards the molecular clouds of higher density. The observed correlation indicates that active regions/ sub-clusters having higher number of YSOs have higher peak A_K value. Fig 16 (left panel) suggests that higher number of YSOs in active regions/ sub-cluster are associated with the higher mass cloud. We presume that massive clouds have higher peak A_K value.

The extinction maps generated in §4.2.1 have been used to estimate the molecular mass associated with the identified sub-clusters/active regions. The A_V value (corrected for the foreground extinction) in each grid of the 30 arc-sec was converted to H_2 column density by using the rela-

tion given by Dickman (1978) and Cardelli et al. (1989), i.e., $N(H_2) = 1.25 \times 10^{21} \times A_V \text{ cm}^{-2} \text{ mag}^{-1}$. The H_2 column density was integrated over the convex hull of each region and multiplied by the H_2 molecule mass to get the cloud mass. The extinction law, $A_K/A_V = 0.09$ (Cohen et al. 1981) has been used to convert A_K values to A_V . The foreground contributions have been corrected for by using the relation: $A_{K_{foreground}} = 0.15 \times D$ (Indebetouw et al. 2005, D is distance in kpc). The properties of the molecular clouds associated with the sub-clusters and active regions are listed in Table 9. The molecular gas associated with the sub-clusters in the present sample shows a wide range in the mass distribution (~ 5.8 to $7621 M_\odot$), with a median value around $\sim 146 M_\odot$. SED analysis would have allowed us to estimate the mass of 489 YSOs (cf. Section 3.3.1), while for other 221 YSOs available data-points are not enough to properly constrain stellar parameters. Hence, the total mass of all the candidate YSOs in the sub-clusters/ active regions has been estimated by multiplying the total number of the YSOs (i.e., 710) with the average SED mass ($2.4 M_\odot$ as discussed in Section 4.1).

An analysis of YSO spacings in sub-clusters of 36 star-forming clusters by Gutermuth et al. (2009) suggested that Jeans fragmentation is a starting point for understanding the primordial structure in SFRs. We estimated the minimum radius required for the gravitational collapse of a homogeneous isothermal sphere (Jeans length ' λ_J ') in order to investigate the fragmentation scale by using the formula given in Chavarría et al. (2014). The Jeans length λ_J estimated for the sub-clusters in the current study has values between 0.8 - 3.3 pc for the sample having Class I and Class II sources as well the sample having assumed missing mass of Class III. The contribution of missing mass of Class III sources has been accounted by assuming a disk fraction of 50%. The resultant number of missed stars has been multiplied with an average SED mass ($2.4 M_\odot$, as discussed in Section 4.1) to get contribution of unidentified Class III sources. The estimated value of Jeans length ' λ_J ' are given in Tables 9 and 10. The median values of ' λ_J ' are estimated as ~ 2 pc for both of the two samples as discussed. We also compared the λ_J and the mean separation ' S_{YSO} ' between the cluster members (Fig. 14, right-hand panel) and found that the ratio λ_J/S_{YSO} has an average value of 3.4 ± 0.9 and 3.2 ± 0.8 for the two samples, respectively. Chavarría et al. (2014) reported the ratio for their sample of embedded clusters as 4.3 ± 1.5 . The present results agree with a non-thermal driven fragmentation since it takes place at scales smaller than the Jeans length (Chavarría et al. 2014).

Lada et al. (2010) have reported that the number of YSOs in a cluster are linearly related to the dense cloud mass $M_{0.8}$ (the mass above a column density equivalent to $A_K \sim 0.8$ mag) with a slope equal to unity. Recently Chavarría et al. (2014) have also found a similar relation for a sample of embedded clusters. This suggests that the star formation rates depend linearly on the mass of the dense cloud (Lada et al. 2010). We also estimated the $M_{0.8}$ (cf. Table 9), accounting only for the Class I and II objects, and found that the number of YSOs in the sub-cluster or active region is linearly correlated with the dense cloud mass with a value of Spearman's correlation coefficient 'r' = 0.8 with 95% confidence interval of 0.6 to 0.9 (cf. Fig. 16, left-hand panel).

The right-hand panel of Fig. 16 shows the hull radius of sub-clusters/ active regions as a function of the total YSO mass, which manifests that the hull radius is linearly correlated ($r=0.8$) to the total YSO mass. The radius versus mass relation gives a clue of whether the cluster will be bound or unbound. The radius limit of a group moving in the Galactic tidal field is defined as the distance from the center of the group at which the attraction of a given star from the cluster is balanced by the tidal force of external masses (Kholopov 1969). The limiting radius r_{lim} for a group that is moving in elliptical orbit around the Galactic center is given by the relation (King 1962).

$$r_{lim} = R_p \left(\frac{M_*}{3.5M_G} \right)^{1/3} \quad (3)$$

where R_p is the perigalactic distance of the group, M_* is the mass of the group and M_G is the mass of the Galaxy. Assuming R_p of the Sun as 8.5 kpc and $M_G \sim 2 \times 10^{11} M_\odot$, the limiting radius r_{lim} as a function of mass of the cluster is shown as the continuous curve in Fig. 16 (right-hand panel). This figure indicates that the radii of all the sub-clusters are below the limiting radius, which suggests that all the sub-clusters will be bound systems, whereas all the active regions may be unbound systems.

4.2.4 Star formation efficiency

The star formation efficiency (SFE), defined as the percentage of the gas mass converted into stars, is an important parameter to determine whether a cluster will be a bound or unbound system etc. Several studies have been carried out, suggesting that the formation of a bound system requires a SFE of $\geq 50\%$ when the gas dispersal is quick or $\geq 30\%$ when the gas dispersal time is ~ 3 Myr (cf. Elmegreen 1983; Lada et al. 1984). Lada et al. (1984) have also concluded that in the case of slow dispersal a lower SFE of $\sim 15\%$ may also produce a bound system.

The observed surface density of the YSOs in the sub-clusters and active regions provides an opportunity to study how this quantity is related to the observed SFE and other properties of the associated molecular cloud. Recent works indicate that SFE increases with the stellar density; e.g., Evans et al. (2009) reported that YSO clusters of higher surface density have higher SFE (30%) than their lower density surroundings (3%-6%). Similarly Koenig et al. (2008) also found SFEs of $>10\%$ -17% for high surface density clusters, whereas in lower density regions the SFEs are found to be $\sim 3\%$. We have calculated the SFE by using the cloud mass derived from A_K inside the cluster convex hull areas and the number of YSOs found in the same areas (see also Koenig et al. 2008). The total mass of the stellar content was estimated as discussed in Section 4.2.3. It is found that for the sub-cluster regions the SFEs varies between 5% to 20% with an average of $\sim 10.2 \pm 1.2\%$. These SFE estimates must be considered as lower limits in these regions as we are considering stellar contents composed of Class I and II sources. Inclusion of Class III sources will increase the SFE values.

In the case of embedded clusters Chavarría et al. (2014) have obtained SFE as 3-45% with an average 20%. The SFE distribution as a function of the number of the cluster mem-

bers and the mean surface density of each of our regions is shown in Fig. 17. The SFE seems to be anti-correlated with the number of the cluster members (Spearman's correlation coefficient 'r' = -0.7 with 95% confidence interval of -0.5 to -0.8) in the sense that the regions associated with high SFEs have smaller numbers of closely packed stars. The right-hand panel of Fig. 17 also indicates a tight correlation between the SFE and mean surface density (Spearman's correlation coefficient 'r' = 0.9 with 95% confidence interval of 0.8 to 1.0) in the sense that the regions having higher YSO densities exhibit higher SFEs. However, Fig. 17 left-hand panel indicates that the regions associated with high SFEs have smaller numbers of stars. The probable explanation for the regions having a smaller number of stars but a higher SFE could be that these regions are closely packed as revealed in Fig. 13.

4.3 Star formation history in the Auriga Bubble region: a series of triggered star formation

Kang et al. (2012) estimated that the shell is expanding with a velocity of ~ 55 km s $^{-1}$ and the kinetic energy of the shell is $\sim 2.5 \times 10^{50}$ ergs. They also detected hard X-ray emitting hot gas inside the shell with a thermal energy of $\sim 3 \times 10^{50}$ ergs. These authors have discussed two possibilities for the formation of this shell, i.e., stellar winds from OB stars and a SN explosion. However, the wind energy of the eight O stars found in the shell cannot explain the large kinetic energy and the hard X-ray emitting hot gas, and so they concluded that a SN created the shell.

As for the origin of H II regions (viz *Sh2* 231 – 235 and *Sh2* 237) within the boundary of the H I/ continuum structure, Kang et al. (2012) discussed that these could have been triggered either by SN explosions, stellar winds, or expanding H II regions by a previous generation of stars. However, since the ages of the H II regions are of the order of a few Myr (see e.g., Jose et al. 2008; Pandey et al. 2013) and the estimated age of the hot shell is only ~ 0.33 Myr, it is not possible that the current expanding shell triggered the formation of these H II regions. They speculated that the first generation massive stars in the stellar association, to which the SN progenitor belonged, could have triggered the formation of the OB stars currently exciting the H II regions.

In a similar line, we propose the following star formation scenario for the Auriga Bubble1 region. The H II complex has several O9 type stars (cf. Table 6, Kang et al. 2012). If one or more of the first generation O9 type stars in the association formed on an expanding H II regions with a large shell around it, after ~ 8 Myr (the MS life time of $20 M_\odot$ O9 type star; Stahler & Palla 2005) the dense material collected around it might have collapsed to form the second generation OB stars (the collect and collapse mechanism advocated by Elmegreen & Lada 1977), which are exciting the current H II regions (i.e., *Sh2* 231 – 235 and *Sh2* 237) around the shell and their associated clusters. Also in a somewhat similar timescale a massive star of the first generation exploded as a SN, forming the shell/Auriga Bubble1.

Fig. 10 manifests that a majority of the Class I and Class II YSOs identified in the present study are located mostly along the boundary of Bubble1 and Bubble2. Their distribution is well correlated with that of the ionized and molecular gas as well as PAHs around the H II complex

G173+1.5. It is interesting to note that [Jose et al. \(2008\)](#) noticed several OB stars around the cluster Stock 8 (associated with Sh2 234) and inferred that these may belong to the group of the first generation in the region. They argued that the OB stars within Stock 8 have ages of 2-3 Myr and were formed by the action of these first generation stars. They also noticed a strange ‘nebulous stream’ towards east of Stock 8, which has a group of very young YSOs (~ 1 Myr) around it, younger than the stars in Stock 8, and argued that the star formation in the nebulous stream region is independent and these very young YSOs belong to a different generation from those in the Stock 8 cluster. They further inferred that these YSOs might have formed in the remaining clouds due to compression by a shock front from the north. Here it is worthwhile to mention that the nebulous stream is located on the Shell/Bubble1 and north is the direction toward the center of the Shell/Bubble1 (see Fig. 5 of [Kang et al. 2012](#)). In addition, a ^{12}CO cloud is found adjacent just to the south of the stream (see Fig. 22 of [Jose et al. 2008](#)).

Based on this fact we propose that most of the youngest YSOs (having ages $\lesssim 1.0$ Myr), identified in the present study as well as those in the nebulous stream are of different origin from the somewhat evolved YSO population located in and around the H II regions and that they may be a SN- triggered population. Fig. 18 (left-hand panel) shows the distribution of the YSOs having ages less than 1.0 Myr. The distribution shows that they are located at the periphery of the Bubbles. Keeping in mind the errors in the age estimation and the distribution of the youngest YSOs along the boundary of the H I and continuum emission, we propose that the expanding Auriga Bubble1 might have compressed the low density molecular material or pre-existing clouds to form a dense shell and this became gravitationally unstable to give birth to a new generation of stars.

Thus the region seems to have a complicated star formation history. It seems that the massive stars of the first generation have mostly completed their lives. One of them made the SN explosion and created Bubble1. The currently ionizing sources of the H II regions located at its periphery (viz Sh2 231 – 235 and Sh2 237) are the results of the triggered star formation through the collect and collapse process by the first generation population. The more or less evolved YSOs around the H II regions are probably stars of the third generation due to the various star formation activities associated with these H II regions. However, the majority of the younger YSOs (having age $\lesssim 1.0$ Myr), located at the periphery of Bubble1 can be of different origin from this YSO population, making another group of the third generation which was formed due to SN-induced compression presumably.

The size of the Bubble is quite large (diameter ~ 100 pc) and it could be one of the largest SNR driven bubbles in the Galaxy. [Kobayashi et al. \(2008\)](#) have also reported a SNR driven shell in the extreme outer Galaxy having an extent of ~ 100 pc, which may also have triggered star formation. This shell has survived for more than 3 Myrs.

The distribution of the YSOs associated with the Bubble1 and 2 region is shown in Fig. 18 (right-hand panel) on the $l-z$ plane. It is interesting to note that a significant number of YSOs are located above the Galactic mid-plane. The center of Bubble1 appears to be ~ 50 pc above the Galactic mid-plane. This seems to be consistent with its warping

around $l \sim 170^\circ - 173^\circ$ toward the northern side. The distribution of the blue plume population around $l \sim 170^\circ$ in the Norma-Cygnus arm also indicates the warping towards the north ([Pandey et al. 2006](#)). The distribution of the large-scale molecular gas ([Nakanishi & Sofue 2006](#)) also reveals the northward warp. The model-based distribution of integrated star light ([Drimmel & Spergel 2001](#)) and red-clump stars ([López-Corredoira et al. 2002](#)) also supports the northward warping of the Galactic plane.

5 CONCLUSION

Using optical observations and archive NIR and MIR data, we have compiled a catalog of 710 YSOs in an area of $6^\circ \times 6^\circ$ around the Auriga Bubble region. Of 710 YSOs 175 and 535 are Class I and Class II YSOs, respectively. The physical parameters of the YSOs were estimated by using SED model fitting. The spatial distribution of the YSOs and the MIR and radio emission have been used to understand the star formation in the region. The followings are the main results:

- The ages of the majority of the YSOs are found to be ≤ 3 Myr, and the masses are in the range of $\sim 3-5 M_\odot$. Twenty five percent (175 out of 710) of the YSOs are Class I sources.
- The spatial distribution of the ionized gas as well as the molecular gas is found to be well correlated with that of the YSOs, which follows two ring-like structures (named as Auriga Bubble 1 and 2) extending over an area of a few degrees each. The majority of the Class I sources are found to be distributed along this structure. Auriga Bubble 1 coincides spatially with the high velocity H I shell discovered by [Kang et al. \(2012\)](#).
- Twenty six probable sub-clusters of the YSOs have been identified on the basis of a MST analysis. The size of the sub-clusters lies in the range of ~ 0.5 pc to ~ 3 pc. The SFE and the limiting radius of these sub-clusters suggest that these may be bound stellar groups.
- We propose the following possible star formation history in the region: the first generation is an already dispersed OB association to which a SN progenitor belonged, whereas the second generation is the current H II regions and their associated clusters; and the more or less evolved YSOs distributed in and around the above H II region belong to the third generation. Further there seems to be another, third generation of YSOs, i.e., the youngest population of the region (ages $\lesssim 1$ Myr). They are distributed along the periphery of the Bubbles and may have been triggered by the SN explosion.
- The center of the bubbles appear to be ~ 50 pc above the Galactic mid-plane.

ACKNOWLEDGMENTS

We are very thankful to the anonymous referee for the critical review of the contents and useful comments. The observations reported in this paper were carried out by using the Schmidt telescope at Kiso Observatory, Japan. We thank the staff members for their assistance during the observations. We are grateful to the DST (India) and JSPS (Japan) for providing financial support to carry out the present study.

We are also thankful to Dr. Neelam Panwar for critical reading of the manuscript and useful discussions. This publication makes use of data products from the Wide-field Infrared Survey Explorer, which is a joint project of the University of California, Los Angeles, and the Jet Propulsion Laboratory/California Institute of Technology, funded by the National Aeronautics and Space Administration. This publication also made use of data from the Two Micron All Sky Survey, which is a joint project of the University of Massachusetts and the Infrared Processing and Analysis Center/California Institute of Technology, funded by the National Aeronautics and Space Administration and the National Science Foundation.

REFERENCES

- Allen L. E., et al., 2004, *ApJS*, **154**, 363
 Allen T. S., et al., 2008, *ApJ*, **675**, 491
 Barsony M., 1994, in Clemens D. P., Barvainis R., eds, *Astronomical Society of the Pacific Conference Series Vol. 65, Clouds, Cores, and Low Mass Stars*. p. 197
 Bastian N., Ercolano B., Gieles M., Rosolowsky E., Scheepmaker R. A., Gutermuth R., Efremov Y., 2007, *MNRAS*, **379**, 1302
 Bastian N., Gieles M., Ercolano B., Gutermuth R., 2009, *MNRAS*, **392**, 868
 Bessell M. S., Brett J. M., 1988, *PASP*, **100**, 1134
 Cardelli J. A., Clayton G. C., Mathis J. S., 1989, *ApJ*, **345**, 245
 Carpenter J. M., Heyer M. H., Snell R. L., 2000, *ApJS*, **130**, 381
 Cartwright A., Whitworth A. P., 2004, *MNRAS*, **348**, 589
 Chavarría L., Allen L., Brunt C., Hora J. L., Muench A., Fazio G., 2014, *MNRAS*, **439**, 3719
 Churchwell E., et al., 2006, *ApJ*, **649**, 759
 Cichowski S., Pineault S., Gamen R., Arnal E. M., Suad L. A., Ortega M. E., 2014, *MNRAS*, **438**, 1089
 Cohen J. G., Persson S. E., Elias J. H., Frogel J. A., 1981, *ApJ*, **249**, 481
 Cutri R. M., et al., 2003, *VizieR Online Data Catalog*, **2246**, 0
 Dame T. M., Hartmann D., Thaddeus P., 2001, *ApJ*, **547**, 792
 Deharveng L., et al., 2012, *A&A*, **546**, A74
 Dickman R. L., 1978, *ApJS*, **37**, 407
 Drimmel R., Spergel D. N., 2001, *ApJ*, **556**, 181
 Elmegreen B. G., 1983, *MNRAS*, **203**, 1011
 Elmegreen B. G., Efremov Y. N., 1997, *ApJ*, **480**, 235
 Elmegreen B. G., Lada C. J., 1977, *ApJ*, **214**, 725
 Elmegreen D. M., et al., 2014, *ApJ*, **787**, L15
 Evans II N. J., et al., 2003, *PASP*, **115**, 965
 Evans II N. J., Dunham M. M., Jørgensen J. K., et al., 2009, *ApJS*, **181**, 321
 Fischer W. J., Padgett D. L., Stapelfeldt K. L., Sewilo M., 2016, *ApJ*, **827**, 96
 Flaherty K. M., Pipher J. L., Megeath S. T., Winston E. M., Gutermuth R. A., Muzerolle J., Allen L. E., Fazio G. G., 2007, *ApJ*, **663**, 1069
 Frail D. A., Mitchell G. F., 1998, *ApJ*, **508**, 690
 Furst E., Reich W., Reich P., Reif K., 1990, *A&AS*, **85**, 691
 Gutermuth R. A., Megeath S. T., Pipher J. L., Williams J. P., Allen L. E., Myers P. C., Raines S. N., 2005, *ApJ*, **632**, 397
 Gutermuth R. A., et al., 2008, *ApJ*, **674**, 336
 Gutermuth R. A., Megeath S. T., Myers P. C., Allen L. E., Pipher J. L., Fazio G. G., 2009, *ApJS*, **184**, 18
 Gutermuth R. A., Pipher J. L., Megeath S. T., Myers P. C., Allen L. E., Allen T. S., 2011, *ApJ*, **739**, 84
 Heyer M. H., et al., 1996, *ApJ*, **464**, L175
 Indebetouw R., Mathis J. S., Babler B. L., et al., 2005, *ApJ*, **619**, 931
 Jose J., et al., 2008, *MNRAS*, **384**, 1675
 Jose J., et al., 2013, *MNRAS*, **432**, 3445
 Jose J., Kim J. S., Herczeg G. J., Samal M. R., Bieging J. H., Meyer M. R., Sherry W. H., 2016, *ApJ*, **822**, 49
 Kang J.-h., Koo B.-C., Salter C., 2012, *AJ*, **143**, 75
 Kholopov P. N., 1969, *Soviet Ast.*, **12**, 625
 King I., 1962, *AJ*, **67**, 471
 Kobayashi N., Yasui C., Tokunaga A. T., Saito M., 2008, *ApJ*, **683**, 178
 Koenig X. P., Leisawitz D. T., 2014, *ApJ*, **791**, 131
 Koenig X. P., Allen L. E., Gutermuth R. A., Hora J. L., Brunt C. M., Muzerolle J., 2008, *ApJ*, **688**, 1142
 Lada C. J., Lada E. A., 2003, *ARA&A*, **41**, 57
 Lada C. J., Margulis M., Dearborn D., 1984, *ApJ*, **285**, 141
 Lada E. A., Bally J., Stark A. A., 1991, *ApJ*, **368**, 432
 Lada C. J., et al., 2006, *AJ*, **131**, 1574
 Lada C. J., Lombardi M., Alves J. F., 2010, *ApJ*, **724**, 687
 Lafon G., Deharveng L., Baudry A., de La Noë J., 1983, *A&A*, **124**, 1
 López-Corredoira M., Cabrera-Lavers A., Garzón F., Hammersley P. L., 2002, *A&A*, **394**, 883
 Marco A., Negueruela I., 2016, *MNRAS*, **459**, 880
 McCray R., Kafatos M., 1987, *ApJ*, **317**, 190
 Mel'Nik A. M., Dambis A. K., 2009, *MNRAS*, **400**, 518
 Meyer M. R., Calvet N., Hillenbrand L. A., 1997, *AJ*, **114**, 288
 Miao J., White G. J., Nelson R., Thompson M., Morgan L., 2006, *MNRAS*, **369**, 143
 Morokuma T., et al., 2014, *PASJ*, **66**, 114
 Nakanishi H., Sofue Y., 2006, *PASJ*, **58**, 847
 Oey M. S., Watson A. M., Kern K., Walth G. L., 2005, *AJ*, **129**, 393
 Ojha D. K., et al., 2004a, *ApJ*, **608**, 797
 Ojha D. K., et al., 2004b, *ApJ*, **616**, 1042
 Pandey A. K., Sharma S., Ogura K., 2006, *MNRAS*, **373**, 255
 Pandey A. K., et al., 2013, *ApJ*, **764**, 172
 Panwar N., Samal M. R., Pandey A. K., Singh H. P., Sharma S., 2019, *AJ*, **157**, 112
 Patel N. A., Goldsmith P. F., Heyer M. H., Snell R. L., Pratap P., 1998, *ApJ*, **507**, 241
 Peeters E., Spoon H. W. W., Tielens A. G. G. M., 2004, *ApJ*, **613**, 986
 Porras A., Christopher M., Allen L., Di Francesco J., Megeath S. T., Myers P. C., 2003, *AJ*, **126**, 1916
 Reach W. T., Rho J., 1999, *ApJ*, **511**, 836
 Reipurth B., Yan C.-H., 2008, *Star Formation and Molecular Clouds towards the Galactic Anti-Center*. p. 869
 Reynoso E. M., Mangum J. G., 2001, *AJ*, **121**, 347
 Ribas Á., Bouy H., Merín B., 2015, *A&A*, **576**, A52
 Richert A. J. W., Getman K. V., Feigelson E. D., Kuhn M. A., Broos P. S., Povich M. S., Bate M. R., Garmire G. P., 2018, *MNRAS*, **477**, 5191
 Robitaille T. P., Whitney B. A., Indebetouw R., Wood K., Denzmore P., 2006, *ApJS*, **167**, 256
 Robitaille T. P., Whitney B. A., Indebetouw R., Wood K., 2007, *ApJS*, **169**, 328
 Sagar R., Richtler T., 1991, *A&A*, **250**, 324
 Sako S., et al., 2012, in *Ground-based and Airborne Instrumentation for Astronomy IV*. p. 84466L, doi:10.1117/12.925765
 Schmeja S., Klessen R. S., 2006, *A&A*, **449**, 151
 Sharma S., Pandey A. K., Ogura K., Mito H., Tarusawa K., Sagar R., 2006, *AJ*, **132**, 1669
 Sharma S., Pandey A. K., Ojha D. K., Chen W. P., Ghosh S. K., Bhattacharya B. C., Maheswar G., Sagar R., 2007, *MNRAS*, **380**, 1141
 Sharma S., Pandey A. K., Ogura K., Aoki T., Pandey K., Sandhu T. S., Sagar R., 2008, *AJ*, **135**, 1934
 Sharma S., et al., 2016, *AJ*, **151**, 126
 Stahler S. W., Palla F., 2005, *The Formation of Stars*
 Stetson P. B., 1987, *PASP*, **99**, 191

- Stetson P. B., 1994, *PASP*, **106**, 250
- Strom K. M., Strom S. E., Merrill K. M., 1993, *ApJ*, **412**, 233
- Szegedi-Elek E., Kun M., Moór A., Marton G., Reipurth B., 2019, *MNRAS*, **484**, 1800
- Ward J. L., Kruijssen J. M. D., 2018, *MNRAS*, **475**, 5659
- Weidner C., Bonnell I. A., Moeckel N., 2011, *MNRAS*, **410**, 1861
- Whitney B. A., Wood K., Bjorkman J. E., Wolff M. J., 2003a, *ApJ*, **591**, 1049
- Whitney B. A., Wood K., Bjorkman J. E., Cohen M., 2003b, *ApJ*, **598**, 1079
- Whitney B. A., Indebetouw R., Bjorkman J. E., Wood K., 2004, *ApJ*, **617**, 1177
- Willis S., Marengo M., Allen L., Fazio G. G., Smith H. A., Carey S., 2013, *ApJ*, **778**, 96
- Wright E. L., et al., 2010, *AJ*, **140**, 1868

Table 1. Log of the optical observations with the Kiso Schmidt telescope.

Date of observations/Filter	Exp. (sec) × No. of frames	Field
06 December 2012		
V	180 × 3,10 × 5	Auriga 1
I	180 × 3,10 × 3	Auriga 1
V	180 × 3,10 × 2	Auriga 2
I	180 × 3,10 × 4	Auriga 2
V	180 × 3,10 × 4	Auriga 3
I	180 × 3,10 × 4	Auriga 3
V	180 × 3,10 × 3	Auriga 5
I	180 × 3,10 × 5	Auriga 5
10 December 2012		
V	180 × 3,10 × 3	Auriga 4
I	180 × 3,10 × 3	Auriga 4
V	180 × 3,10 × 4	Auriga 6
I	180 × 3,10 × 3	Auriga 6
27 December 2014		
V	180 × 5	Auriga 7
I	180 × 7	Auriga 7
V	180 × 3	Auriga 8
I	180 × 7	Auriga 8
V	180 × 10	Auriga 9
I	180 × 9	Auriga 9

Table 2. Values of the coefficients for calibrating different Auriga fields.

Calibrated Field - Standard Field	Long Exposures				Short Exposures			
	M1	C1	M2	C2	M1	C1	M2	C2
Auriga 1 - NGC 1960	0.013 ± 0.002	3.354 ± 0.003	1.003 ± 0.002	0.396 ± 0.002	0.018 ± 0.002	0.208 ± 0.002	1.032 ± 0.002	0.354 ± 0.002
Auriga 3 - NGC 1960	0.022 ± 0.002	3.346 ± 0.003	1.029 ± 0.002	0.342 ± 0.002	0.028 ± 0.002	0.157 ± 0.002	1.058 ± 0.002	0.305 ± 0.002
Auriga 2 - Auriga 1	0.042 ± 0.002	3.259 ± 0.003	0.995 ± 0.004	0.261 ± 0.005	0.028 ± 0.003	0.173 ± 0.003	0.994 ± 0.005	0.396 ± 0.004
Auriga 4 - Auriga 2	0.046 ± 0.001	3.156 ± 0.001	0.986 ± 0.002	0.164 ± 0.003	0.057 ± 0.002	0.143 ± 0.002	0.990 ± 0.003	0.357 ± 0.002
Auriga 6 - Auriga 4	0.049 ± 0.001	3.306 ± 0.001	0.984 ± 0.002	0.289 ± 0.002	0.091 ± 0.003	0.123 ± 0.002	1.017 ± 0.003	0.241 ± 0.002
Auriga 5 - Auriga 6	0.054 ± 0.005	2.970 ± 0.006	0.972 ± 0.003	0.120 ± 0.003	0.056 ± 0.007	-0.06 ± 0.007	0.961 ± 0.006	0.304 ± 0.004
Auriga 3 - Auriga 5	0.083 ± 0.004	3.289 ± 0.004	0.957 ± 0.004	0.373 ± 0.003	0.056 ± 0.005	0.095 ± 0.005	0.967 ± 0.004	0.328 ± 0.003
Auriga 8 - Auriga 4	0.053 ± 0.001	3.101 ± 0.003	0.978 ± 0.002	0.184 ± 0.002	—	—	—	—
Auriga 7 - Auriga 6	0.101 ± 0.001	3.194 ± 0.001	0.988 ± 0.001	0.288 ± 0.002	—	—	—	—
Auriga 9 - Auriga 2	0.053 ± 0.002	3.389 ± 0.002	0.968 ± 0.003	0.652 ± 0.002	—	—	—	—

$$V - v = M1 \times (V - I) + C1$$

$$(V - I) = M2 \times (v - i) + C2$$

Table 3. Comparison of the photometric calibration for the Auriga 1 field done with the data from NGC 1960 (Sharma et al. 2006) and that done with the Auriga 3 data as explained in Section 2.1. Δ represents the difference of NGC 1960 calibration - Auriga 3 calibration.

V range	N	$\Delta(V) \pm \sigma$	$\Delta(V - I) \pm \sigma$
9.5-10.5	69	-0.018 ± 0.020	0.046 ± 0.036
10.5-11.5	175	-0.014 ± 0.022	0.039 ± 0.040
11.5-12.5	406	-0.006 ± 0.025	0.025 ± 0.044
12.5-13.5	867	-0.001 ± 0.024	0.017 ± 0.043
13.5-14.5	1584	0.001 ± 0.020	0.008 ± 0.025
14.5-15.5	3163	0.008 ± 0.021	-0.002 ± 0.026
15.5-16.5	5486	0.016 ± 0.021	-0.011 ± 0.026
16.5-17.5	8644	0.023 ± 0.020	-0.020 ± 0.024
17.5-18.5	12098	0.032 ± 0.018	-0.031 ± 0.023
18.5-19.5	13350	0.043 ± 0.019	-0.044 ± 0.023

Table 4. Same as Table 3 but for comparison of the photometric calibration of common stars in the Auriga 1 and Auriga 3 fields done by using the data of NGC 1960.

V range	N	$\Delta(V) \pm \sigma$	$\Delta(V - I) \pm \sigma$
9.5-10.5	12	0.034 ± 0.042	-0.066 ± 0.038
10.5-11.5	31	0.042 ± 0.030	-0.046 ± 0.031
11.5-12.5	92	0.029 ± 0.045	-0.033 ± 0.061
12.5-13.5	182	0.009 ± 0.048	-0.033 ± 0.071
13.5-14.5	290	-0.008 ± 0.037	-0.011 ± 0.043
14.5-15.5	614	-0.026 ± 0.048	-0.009 ± 0.054
15.5-16.5	1039	-0.039 ± 0.054	0.002 ± 0.058
16.5-17.5	1636	-0.047 ± 0.059	0.012 ± 0.066
17.5-18.5	2317	-0.040 ± 0.067	0.037 ± 0.074
18.5-19.5	2182	-0.027 ± 0.095	0.074 ± 0.108

Table 5. Sample of 710 identified YSOs along with their optical (present study), NIR (2MASS) and MIR (*WISE*) bands magnitudes and errors. The complete table is available as online supplementary material.

ID	RA	Dec	$V \pm \sigma$	$I \pm \sigma$	$J \pm \sigma$	$H \pm \sigma$	$K \pm \sigma$	$W1 \pm \sigma$	$W2 \pm \sigma$	$W3 \pm \sigma$	$W4 \pm \sigma$	Classification*
1	79.530584	+38.373309	–	–	15.507 ± 0.080	$14.092 \pm$	$13.460 \pm$	12.487 ± 0.025	11.475 ± 0.022	8.064 ± 0.022	5.554 ± 0.042	1
2	79.549134	+37.034571	–	–	16.615 ± 0.131	15.082 ± 0.077	13.607 ± 0.042	10.999 ± 0.024	9.826 ± 0.021	7.136 ± 0.017	4.802 ± 0.032	1
3	79.710650	+38.903351	–	–	16.282 ± 0.101	15.184 ± 0.089	14.163 ± 0.057	12.366 ± 0.023	11.287 ± 0.022	7.950 ± 0.021	5.164 ± 0.031	1
4	79.753427	+36.830059	–	–	14.120 ± 0.031	13.081 ± 0.033	12.348 ± 0.028	11.000 ± 0.023	9.762 ± 0.021	6.491 ± 0.016	4.228 ± 0.022	1
5	79.765052	+36.770991	–	–	14.301 ± 0.036	12.597 ± 0.033	11.018 ± 0.026	9.051 ± 0.022	7.530 ± 0.021	4.630 ± 0.014	2.655 ± 0.018	1

*: Classification of YSOs i.e., 1=Class I (WISE 3 Band), 2=Class II (WISE 3 Band), 3=Class I (WISE+2MASS, two Band each), 4=Class II (WISE+2MASS, two Band each), 5=Class I (from AGN contamination list), 6=Class II (WISE 4 BAND, Tr Disk), 7=Class I (2MASS TCD), 8=Class II (2MASS TCD).

Table 6. Summary of the limiting magnitude and completeness limit for each band.

Band	Sources in the Auriga Region	Detection Limit (mag)	90% Completeness Limit (mag)
V	470876	21.21	19.00
I	470876	20.03	17.75
J	550210	17.31	15.80
H	538281	15.51	15.10
K	500720	14.55	14.30
W1	696985	17.06	15.75
W2	671510	17.30	15.50
W3	50900	11.71	11.25
W4	1001	6.80	6.25

Table 7. A sample table containing the stellar parameters of the selected 489 YSOs derived by using the SED fitting analysis. IDs are the same as in Table 5. The complete table is available as online supplementary material.

IDs	N	Model	χ^2	A_V (mag)	Mass (M_\odot)	Age (Mys)
1	7	501	1.8	6.5 ± 4.1	1.3 ± 1.2	1.2 ± 2.2
2	7	213	2.7	12.0 ± 4.7	2.9 ± 1.1	4.4 ± 2.7
3	7	263	1.5	3.5 ± 3.0	0.9 ± 1.0	0.6 ± 2.3
4	7	243	2.6	6.1 ± 3.1	3.2 ± 1.6	2.3 ± 2.1
5	7	334	1.3	8.0 ± 3.0	4.6 ± 1.6	2.7 ± 2.2

Table 8. Data for identified sub-clusters and active regions. Columns 2 and 3 are their center coordinates. The total number of YSOs and their distribution as a function of their evolutionary status are given in column 4 and columns 13 to 15, respectively. The hull and circle radius along with the aspect ratio are given in columns 6, 7 and 8, respectively. Columns 9 and 10 represent the mean and peak stellar density, respectively, obtained by using the isodensity contours. Columns 11 and 12 are the mean MST branch length and NN distances, respectively.

Name	$\alpha_{(2000)}$ ($h:m:s$)	$\delta_{(2000)}$ ($^{\circ}:'''$)	N^a	V^b	R_{hull} (pc)	R_{cir} (pc)	Aspect Ratio	σ_{mean} (pc^{-2})	σ_{peak} (pc^{-2})	MST ^c (pc)	NN2 ^c (pc)	Class I	Class II	Frac ^d (%)
Sub-clusters														
g0	05:27:06.528	+38:31:00.69	7	5	0.57	0.80	1.96	6.81	4.00	0.18	0.13	2	5	29
g1	05:33:44.632	+37:18:09.48	36	7	2.98	4.13	1.92	1.29	12.59	0.47	0.34	6	30	17
g2	05:36:25.763	+36:39:57.65	11	7	1.15	1.21	1.11	2.64	7.58	0.39	0.36	1	10	9
g3	05:36:14.706	+36:29:12.13	5	4	1.51	1.72	1.30	0.70	0.49	0.41	0.22	2	3	40
g4	05:36:51.731	+36:10:47.44	7	5	0.83	0.95	1.30	3.24	8.19	0.25	0.22	3	4	43
g5	05:37:19.582	+36:24:39.27	5	4	0.46	1.24	7.22	7.45	0.00	0.17	0.12	1	4	20
g6	05:37:57.437	+36:01:19.43	17	7	2.19	4.37	4.00	1.13	5.07	0.68	0.41	12	5	71
g7	05:38:56.528	+36:01:34.84	15	7	3.28	2.84	0.75	0.44	1.63	1.10	0.89	5	10	33
g8	05:40:43.580	+35:55:49.86	13	6	2.21	2.03	0.85	0.85	2.79	0.71	0.54	4	9	31
g9	05:41:03.392	+35:44:52.26	79	7	5.05	6.52	1.67	0.99	17.70	0.48	0.28	18	61	23
g10	05:40:43.951	+35:26:31.58	7	5	1.90	1.53	0.65	0.62	1.84	0.78	0.50	1	6	14
g11	05:41:20.297	+36:09:24.94	7	6	1.70	1.44	0.72	0.77	8.42	0.36	0.30	2	5	29
g12	05:41:23.041	+36:18:05.91	5	3	0.48	0.81	2.86	6.89	1.63	0.47	0.30	2	3	40
g13	05:38:51.456	+33:41:33.88	9	6	1.46	1.78	1.50	1.35	2.24	0.33	0.25	3	6	33
g14	05:24:39.753	+35:02:36.77	7	4	1.44	1.82	1.59	1.07	1.68	0.52	0.45	0	7	0
g15	05:25:25.517	+34:58:04.70	11	6	1.56	2.02	1.67	1.43	8.91	0.53	0.22	3	8	27
g16	05:25:49.676	+34:52:46.42	5	4	1.50	1.54	1.05	0.71	4.28	0.77	0.93	1	4	20
g17	05:26:47.987	+35:08:53.74	5	3	0.80	0.85	1.12	2.48	1.79	0.55	0.35	1	4	20
g18	05:28:06.715	+34:24:34.32	18	4	2.22	3.09	1.94	1.16	4.17	0.64	0.41	2	16	11
g19	05:28:57.746	+34:23:10.62	15	8	1.23	2.49	4.10	3.17	6.33	0.33	0.26	1	14	7
g20	05:30:48.071	+33:47:43.60	5	3	0.49	0.85	3.05	6.73	2.00	0.43	0.23	0	5	0
g21	05:31:25.302	+34:13:04.01	6	5	1.65	1.73	1.11	0.71	0.74	0.75	0.60	0	6	0
g22	05:22:55.492	+33:28:58.03	22	7	2.15	2.77	1.66	1.51	5.07	0.51	0.45	0	22	0
g23	05:21:53.771	+36:38:38.55	9	5	1.25	1.76	1.97	1.83	6.60	0.45	0.26	3	6	33
g24	05:21:06.340	+36:39:20.86	10	6	1.14	1.85	2.66	2.47	6.90	0.37	0.26	4	6	40
g25	05:20:20.546	+36:37:10.68	9	5	1.34	1.31	0.95	1.59	2.79	0.50	0.30	4	5	44
Active regions														
g26	05:30:11.112	+38:18:03.20	66	10	22.96	42.82	3.48	0.04	5.24	2.63	1.19	26	40	39
g27	05:33:42.774	+37:17:49.50	40	6	5.05	7.71	2.34	0.50	12.59	0.52	0.36	3	33	8
g28	05:39:39.651	+35:57:23.56	220	9	30.96	39.23	1.61	0.07	17.70	0.69	0.49	64	156	29
g29	05:39:42.971	+34:19:10.29	19	9	17.40	21.44	1.52	0.02	0.06	4.50	3.02	5	14	26
g30	05:39:09.134	+33:37:16.20	16	7	4.86	8.19	2.84	0.22	2.24	0.77	0.33	5	11	31
g31	05:30:12.869	+36:49:49.87	11	6	11.41	14.68	1.66	0.03	0.90	4.37	1.35	1	10	9
g32	05:26:58.099	+34:41:14.16	110	10	21.13	30.04	2.02	0.08	10.09	1.01	0.64	16	94	15
g33	05:22:52.650	+33:29:09.24	25	5	4.81	6.61	1.89	0.34	5.07	0.54	0.46	1	24	4
g34	05:20:44.558	+36:39:37.74	38	7	9.06	12.42	1.88	0.15	10.09	0.72	0.45	13	25	34

a: Number of YSOs enclosed in the group; b: Vertex of the convex hull; c: Median branch length; d: Ratio of Class I/(Class I + Class II)

Table 9. Properties of the identified sub-clusters and active regions. The mean and peak extinction values are given in Columns 2 and 3, respectively. Column 4 represents the cloud mass in the convex hull derived by using the extinction map. Column 5 gives the mass of the dense cloud having A_K greater than 0.8 mag. Columns 6/7, 8, 9/10 and 11/12 represent the Jeans length, Q value, SFE, and ratio of the Jeans length to the mean separation of YSOs, respectively.

Name	$A_{V_{mean}}$ (mag)	$A_{V_{peak}}$ (mag)	Mass (M_{\odot})	Mass $_{0.8}$ (M_{\odot})	Jeans length (pc) J1*	J2**	Q	SFE1*	SFE2**	J/S_{YSO} *	J/S_{YSO} **
Sub-clusters											
g0	6.7	8.7	10.3	-	1.76	1.48	0.60	61.5	76.2	5.6	4.7
g1	9.2	17.8	1688.8	708.2	2.10	2.08	0.59	4.8	9.1	3.9	3.9
g2	8.4	14.3	96.7	12.9	2.02	1.92	0.83	21.1	34.8	4.6	4.4
g3	11.3	15.8	127.8	88.3	2.73	2.68	0.67	8.4	15.5	2.8	2.8
g4	13.9	16.4	50.0	50.0	1.70	1.60	0.86	24.8	39.7	3.7	3.5
g5	-	-	-	-	-	-	-	-	-	-	-
g6	10.8	18.8	867.2	611.4	1.85	1.83	0.53	4.4	8.4	2.3	2.3
g7	10.1	16.6	1576.7	829.5	2.53	2.52	0.79	2.2	4.3	2.4	2.4
g8	11.5	22.7	798.6	558.6	1.96	1.94	0.80	3.7	7.1	2.5	2.5
g9	12.1	22.5	7621.0	5930.7	2.20	2.18	0.61	2.4	4.6	4.0	3.9
g10	9.7	13.9	265.7	131.6	2.69	2.66	0.84	5.8	11.0	3.0	3.0
g11	10.8	19.0	131.6	92.4	3.20	3.12	0.66	11.1	20.0	5.3	5.1
g12	7.3	7.3	5.8	-	1.72	1.42	0.76	67.0	80.2	3.6	2.9
g13	7.6	10.7	140.5	18.4	2.45	2.38	0.66	13.1	23.1	3.9	3.7
g14	10.3	14.9	222.3	103.6	1.94	1.91	0.71	6.9	12.9	2.4	2.4
g15	9.6	13.7	268.6	148.0	1.98	1.94	0.66	8.8	16.1	3.2	3.1
g16	10.3	15.3	106.0	56.4	2.96	2.90	0.83	10.0	18.1	2.9	2.9
g17	10.6	12.9	73.3	42.3	1.37	1.33	0.81	13.8	24.3	2.2	2.2
g18	6.6	12.9	601.1	72.1	2.26	2.22	0.70	6.6	12.3	3.2	3.1
g19	9.9	17.4	195.6	101.2	1.60	1.54	0.45	15.3	26.5	3.8	3.7
g20	13.7	16.1	49.4	49.4	0.79	0.76	0.71	19.2	32.2	1.7	1.6
g21	8.4	11.9	110.6	40.3	3.33	3.25	0.70	11.3	20.3	3.9	3.8
g22	7.3	13.4	563.0	129.3	2.21	2.17	0.71	8.4	15.5	3.8	3.7
g23	10.1	15.1	199.3	98.5	1.64	1.61	0.71	9.6	17.5	2.8	2.7
g24	10.5	14.1	145.7	89.1	1.66	1.61	0.68	13.9	24.4	3.3	3.2
g25	9.6	14.6	196.8	111.8	1.84	1.80	0.79	9.7	17.7	3.0	2.9
Active regions											
g26	5.8	17.6	64530.5	4674.1	7.35	7.35	0.40	0.2	0.5	2.6	2.6
g27	7.8	17.8	4185.3	925.2	2.96	2.95	0.75	2.2	4.3	3.7	3.7
g28	7.9	24.1	182462.2	53738.4	6.84	6.84	0.52	0.3	0.6	4.7	4.7
g29	6.1	15.4	22525.6	1537.7	8.21	8.20	0.67	0.2	0.4	1.7	1.7
g30	6.1	19.5	1905.0	176.1	4.15	4.13	0.50	1.9	3.8	2.9	2.9
g31	6.2	15.7	9304.3	649.5	6.78	6.78	0.67	0.3	0.6	1.5	1.5
g32	6.4	24.5	61706.7	5518.6	6.63	6.63	0.50	0.4	0.8	3.8	3.8
g33	6.8	15.1	3047.0	419.7	3.23	3.22	0.99	1.9	3.7	2.7	2.7
g34	6.4	17.1	10179.2	1095.2	4.58	4.57	0.48	0.9	1.7	3.5	3.5

*: For Class I and Class II sources only.

** : With inclusion of assumed missing contribution of Class III sources.

Table 10. Median value of the parameters of all the sub-clusters and active regions.

Properties	Sub-cluster	Active region
Number of YSOs	9	38
R_{hull} (pc)	1.5	11.4
Aspect Ratio	1.6	1.9
Mean number density (pc^{-2})	1.4	0.1
Peak number density (pc^{-2})	4	5.1
A_K (mag)	0.9	0.6
Peak A_K (mag)	1.3	1.6
Cloud mass (M_{\odot})	146	10179
Dense cloud mass (M_{\odot})	99	1095
MST branch length (pc)	0.47	0.77
Structural Q parameter	0.71	0.52
Jeans Length (pc)	2.0 (1.9)*	6.6 (6.6)*
Star formation efficiency (%)	9.7 (17.7)*	0.4 (0.8)*

*: Values within parenthesis are the estimates with inclusion of assumed contribution of Class III sources.

This paper has been typeset from a $\text{T}_{\text{E}}\text{X}/\text{L}^{\text{A}}\text{T}_{\text{E}}\text{X}$ file prepared by the author.

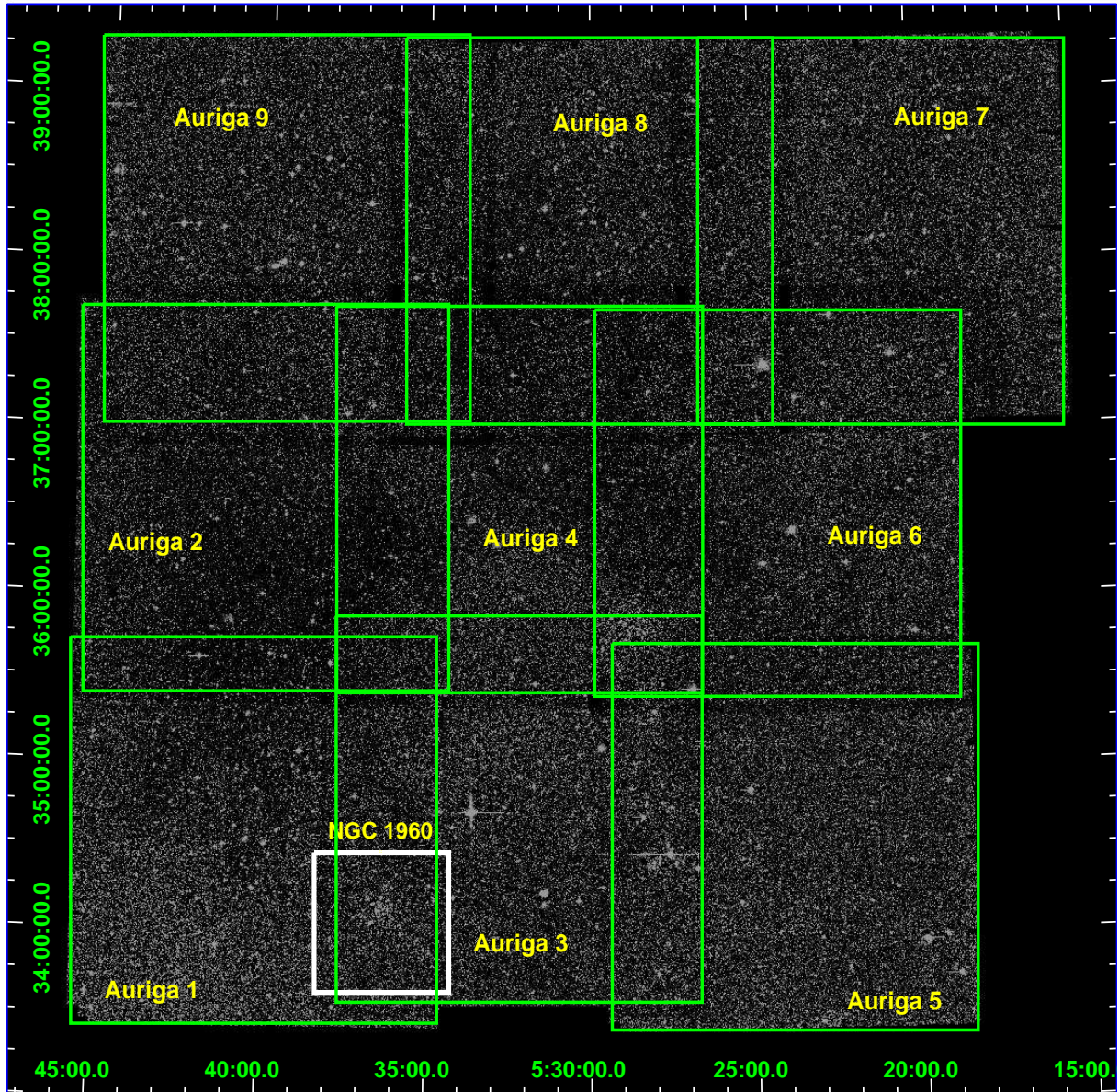


Figure 1. The observed region ($\sim 6 \times 6$ degree²) of Auriga. The nine pointings (green boxes) along with the standard field (NGC 1960: white box) are also shown.

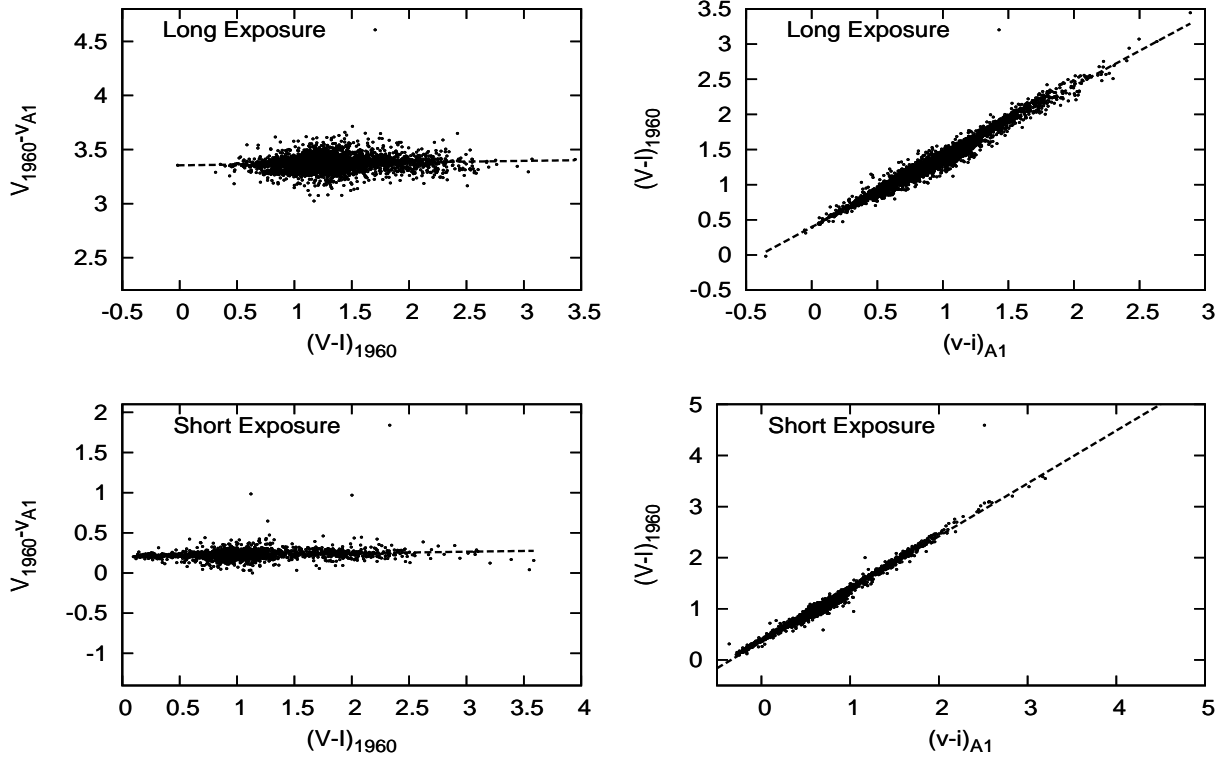


Figure 2. Calibration of the Auriga Bubble1 region using the stars in the cluster NGC 1960 from [Sharma et al. \(2006\)](#) as standard stars for long and short exposures separately. The subscripts 1960 and A1 represent the calibrated magnitudes/colours of stars in NGC 1960 and the present instrumental magnitudes/colours of stars in Auriga A1, respectively.

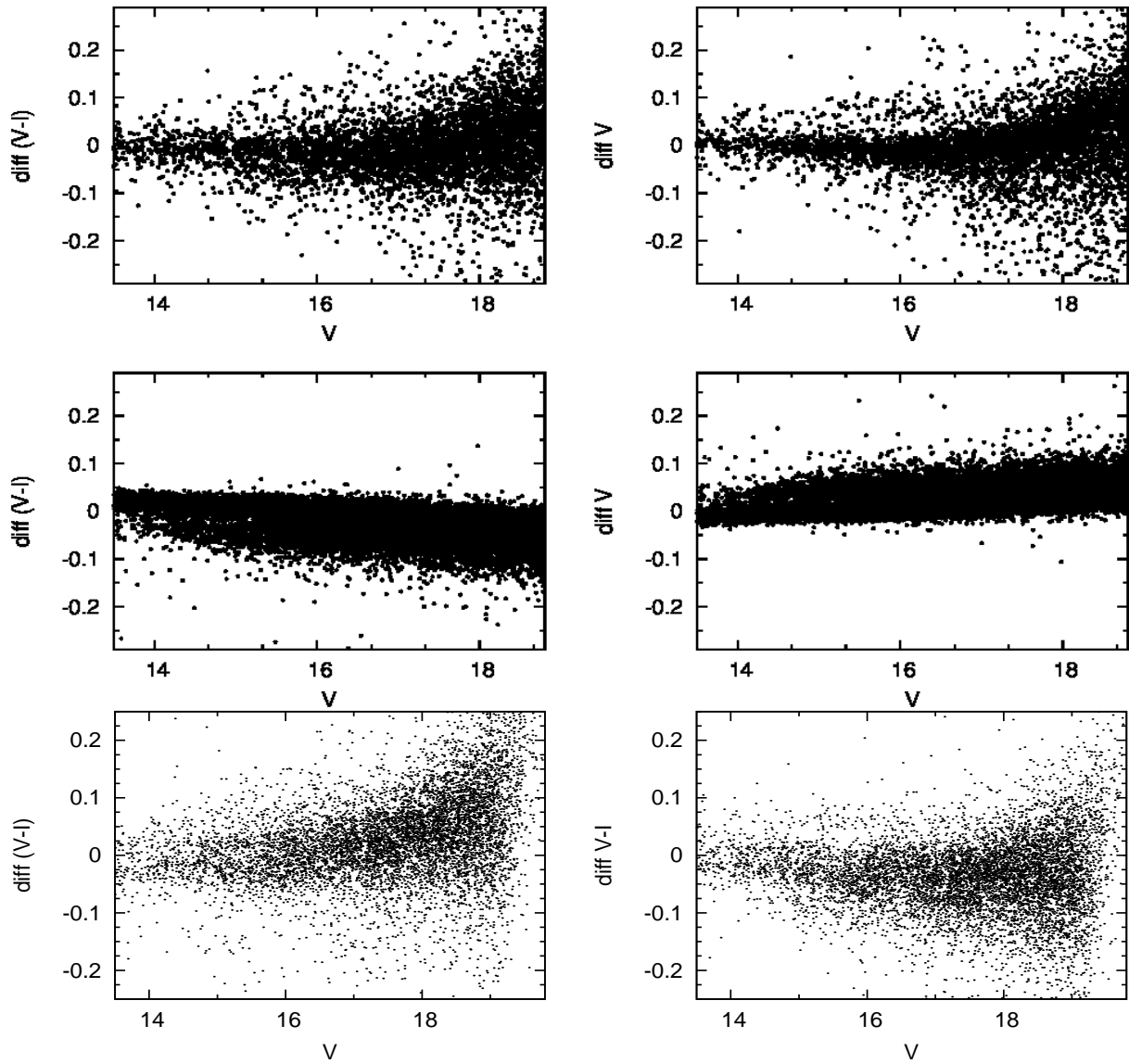


Figure 3. Differences between the calibrated colours and magnitudes as a function of V magnitude. Top panels show the difference between the NGC 1960 cluster data in Auriga 1 field (calibrated by using the data by [Sharma et al. \(2006\)](#)) and the NGC 1960 data, whereas middle panels plot the difference between the Auriga 1 field data calibrated by using NGC 1960 and those calibrated by using the common stars in Auriga 1 and Auriga 3, cf. Table 3). The lower panel compares the photometry of common stars (calibrated by using the NGC 1960 data) of Auriga 1 and Auriga 3 (cf. Table 4).

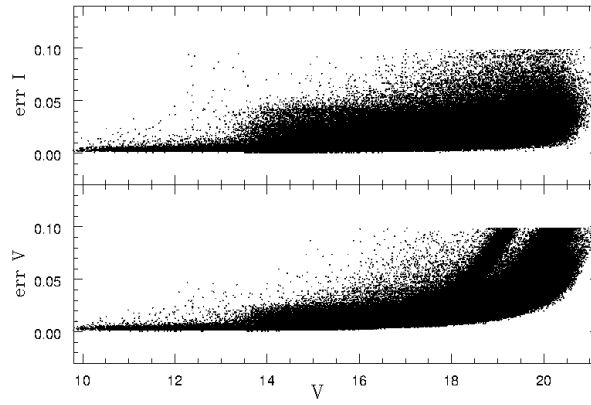


Figure 4. DAOPHOT errors as a function of V magnitude. The data for $V < 13.5$ and $V > 13.5$ are taken from short and long exposures, respectively.

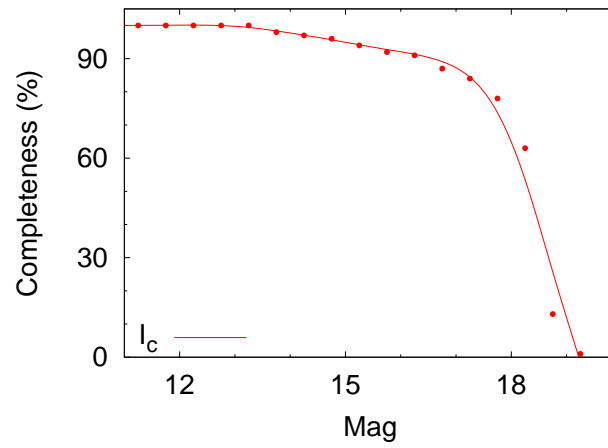


Figure 5. Completeness levels for I_c band as a function of magnitude derived from the artificial star experiments (see Section 3.2 for details).

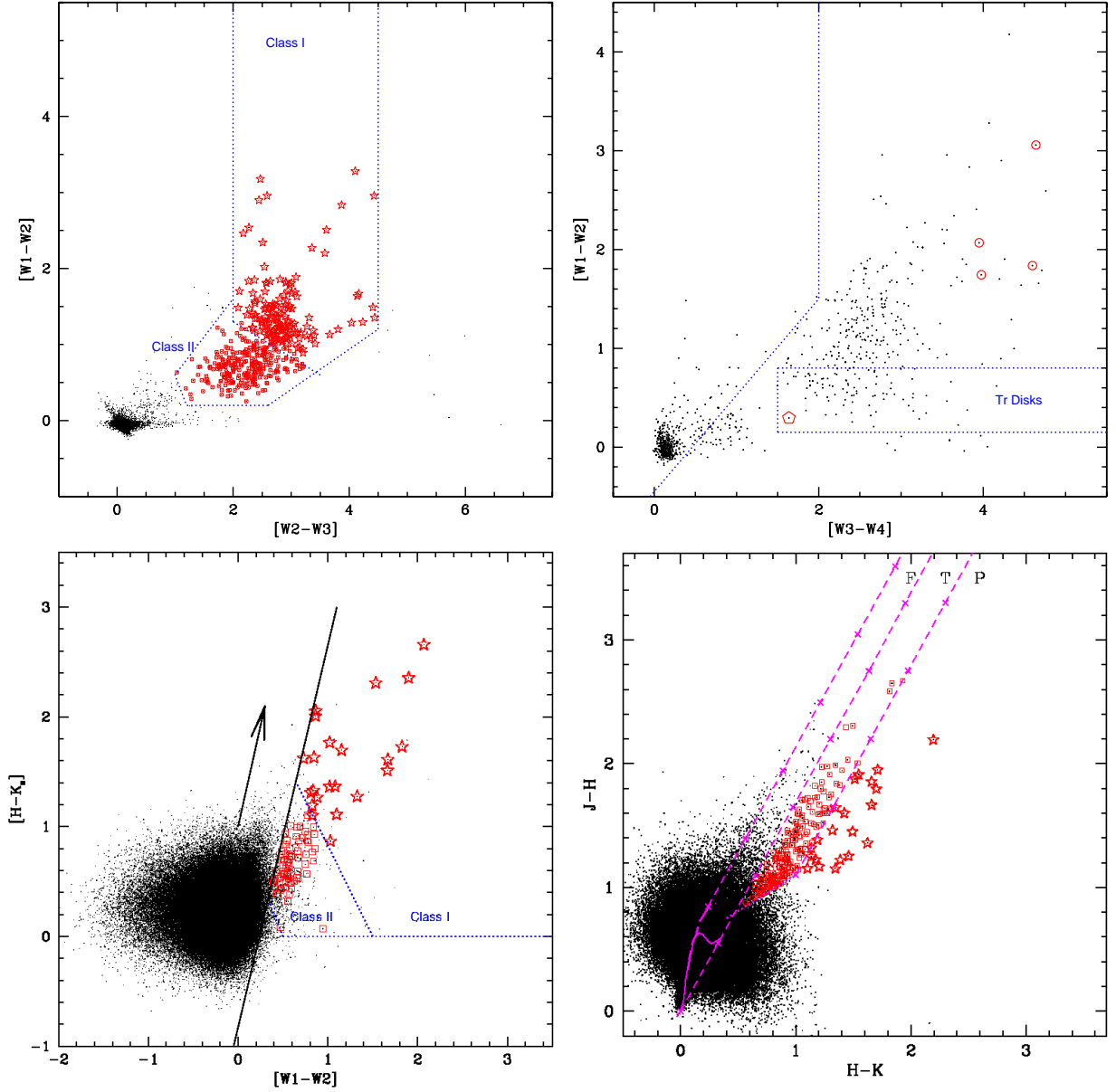


Figure 6. WISE/2MASS TCDs of all the sources within the studied region (black dots). The YSOs classified as Class I, Class II, and transition disk stars on the basis of colour criteria by Koenig & Leisawitz (2014) and Ojha et al. (2004a) are shown with stars, squares, and pentagon symbols, respectively. Dotted lines show the YSO Class divisions. An arrow in bottom-left panel shows the extinction vector of $A_{KS} = 2$ mag. In the same panel, the solid black line parallel to the extinction vector represents the highest range of extinctions tabulated in Table 10 of Koenig & Leisawitz (2014). The continuous and thick magenta dashed curves in the bottom right-hand panel represent the intrinsic main sequence (MS) and giant branches (Bessell & Brett 1988), respectively. The dotted line indicates the loci of unreddened CTTSs (Meyer et al. 1997). The parallel magenta dashed lines in the same panel are the reddening lines drawn from the tip (spectral type M4) of the giant branch (left reddening line), from the base (spectral type A0) of the MS branch (middle reddening line) and from the tip of the intrinsic CTTS line (right reddening line). The crosses on the reddening lines show an increment of $A_V = 5$ mag.

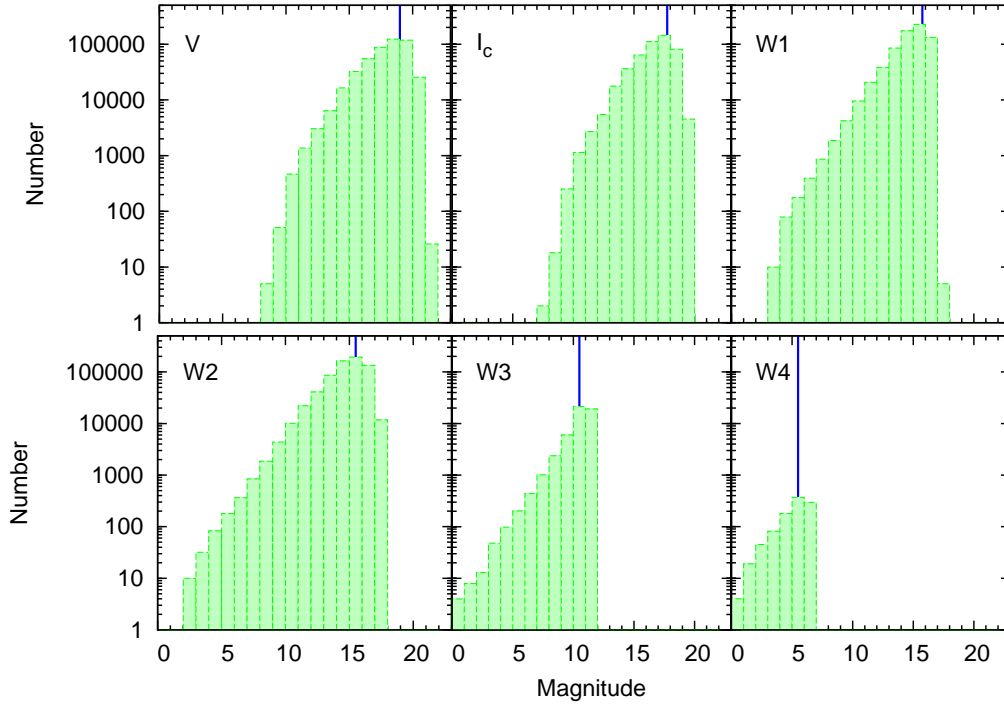


Figure 7. Histograms of the source numbers for different bands showing the limiting magnitude and completeness limit for each band. The vertical lines indicate the adopted completeness limit.

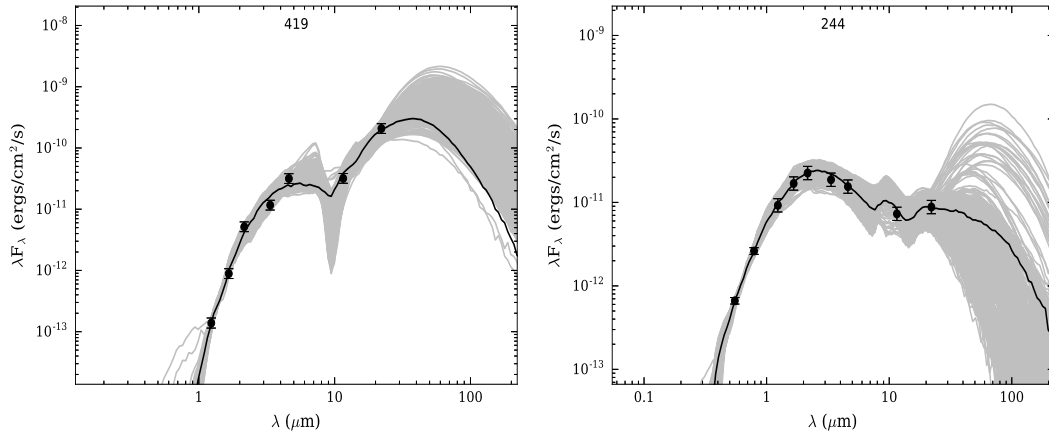


Figure 8. Sample SEDs for Class I (left-hand panel) and Class II (right-hand panel) sources, respectively, created by the SED fitting tools of Robitaille et al. (2007). The black curve shows the best fit and the gray curves show the subsequent well fits satisfying our selection criteria (see text for details). The filled circles with error bars denote the input flux values.

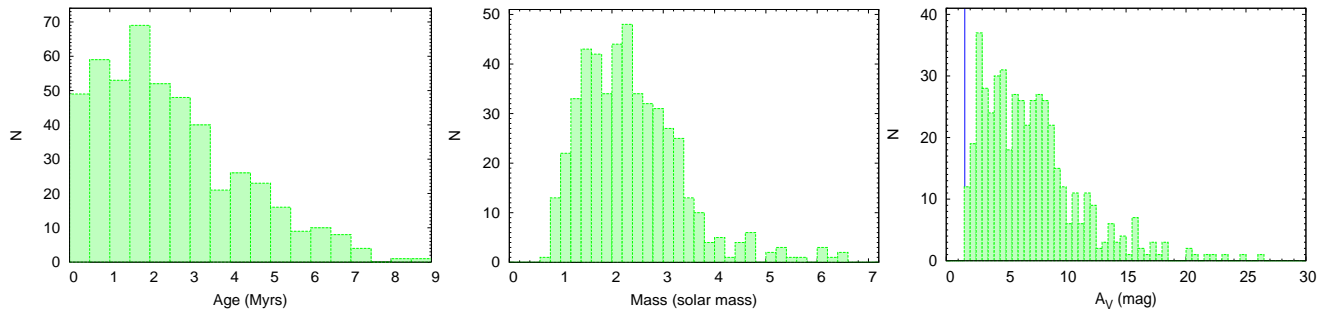


Figure 9. Histograms showing the distribution of the ages (left panel), masses (middle panel) and extinction values ‘ A_V ’ (right panel), respectively, of the YSOs in the Auriga Bubble region. A vertical line in the right panel indicates the foreground reddening value (i.e. $A_V = 1.55$ mag).

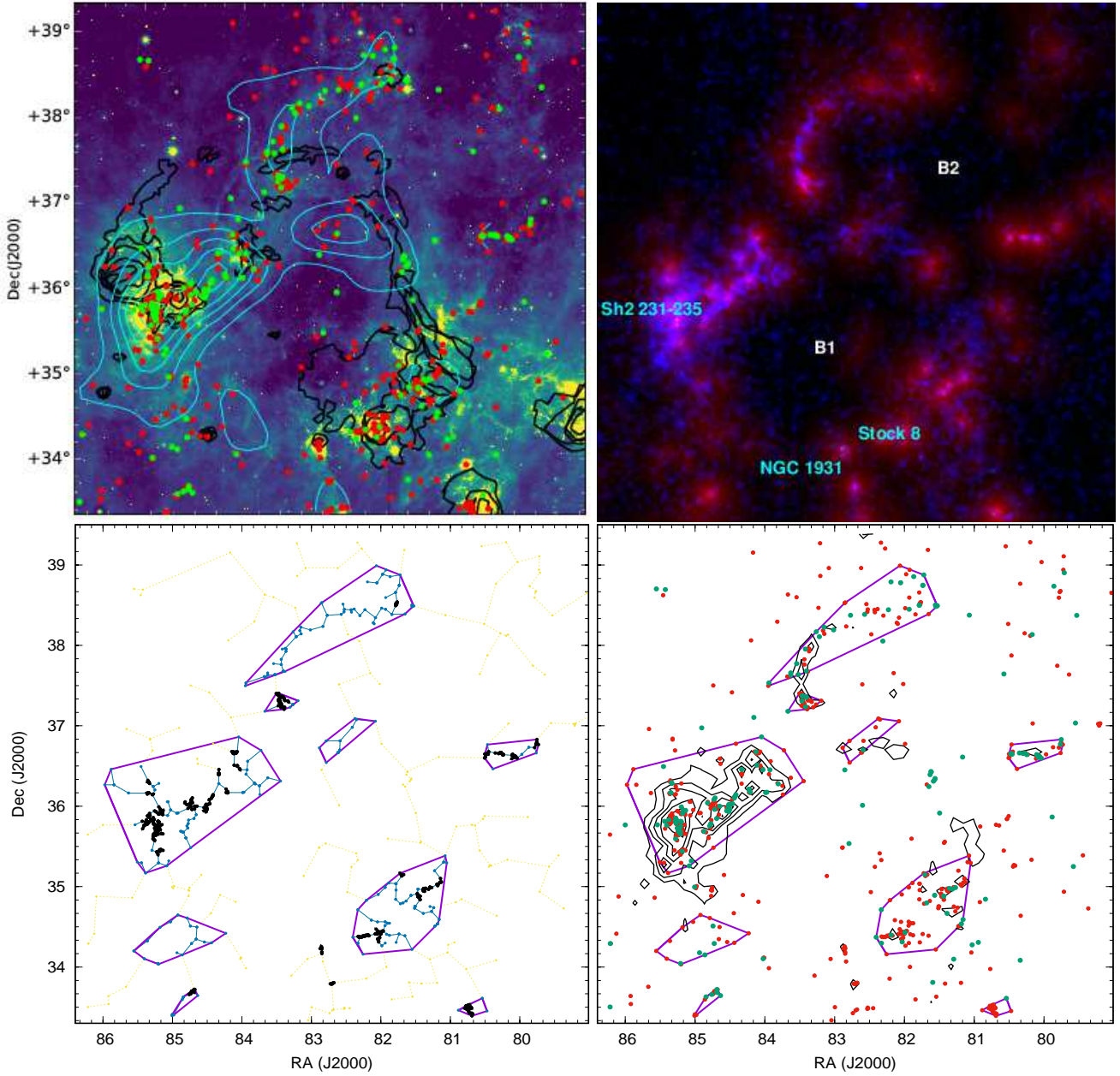


Figure 10. Top left-hand panel: Spatial distribution of YSOs superimposed on the $6^\circ \times 6^\circ$ *WISE* $12\ \mu\text{m}$ image of the Auriga Bubble region. Class I (175) and Class II (535) YSOs are shown by green and red dots, respectively. The cyan and black curves are the ^{12}CO and H I contours taken from Dame et al. (2001) and Furst et al. (1990), respectively. Top right-hand panel: Extinction map (blue colour) and YSOs density map (red colour) for the Auriga Bubble region smoothed to a resolution of 18 arcmin. Bottom left-hand panel: MST for the identified YSOs in the Auriga Bubble region along with the convex hull for active regions. The black dots connected with solid black lines and the blue dots connected with blue solid lines are the branches smaller than the critical length for the sub-clusters and the active regions, respectively. The identified active regions are encircled with purple solid lines. Bottom right-hand panel: The identified active regions along with the extinction contours (black) and the YSOs distribution.

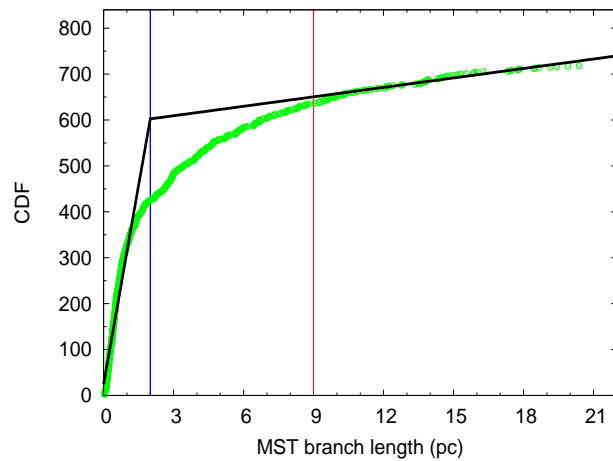


Figure 11. CDF of MST branch lengths used for the critical length analysis. The black solid line is a two-line fit to the CDF distribution. The inner and outer vertical lines stand for the critical lengths obtained for sub-clusters and active regions, respectively.

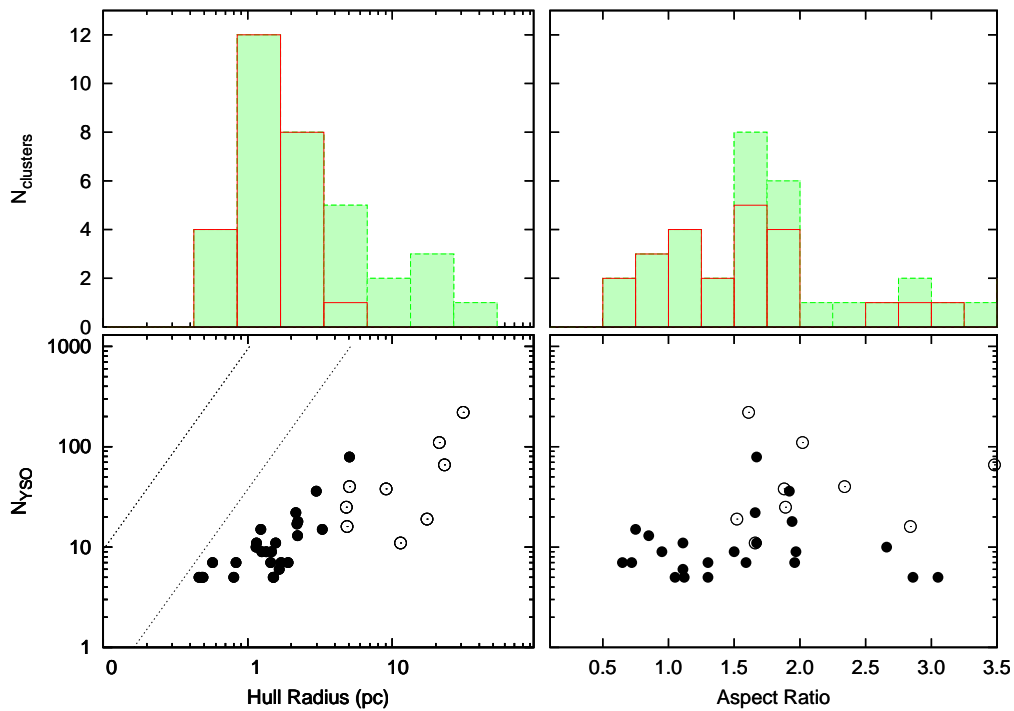


Figure 12. Histogram showing the hull radius distribution (upper left-hand panel) and plot of the hull radius versus the number of cluster members (lower left-hand panel). The red solid histogram and filled circles are for the sub-clusters, and the green dotted histogram and open circles are for the active regions. The dotted lines in the lower-left panel represent the constant surface densities at 12 and 300 pc^{-2} . Those correspond to the range spanned by the embedded clusters from [Gutermuth et al. \(2009\)](#). Right-hand panels: Same as the left-hand, but for the aspect ratio distribution.

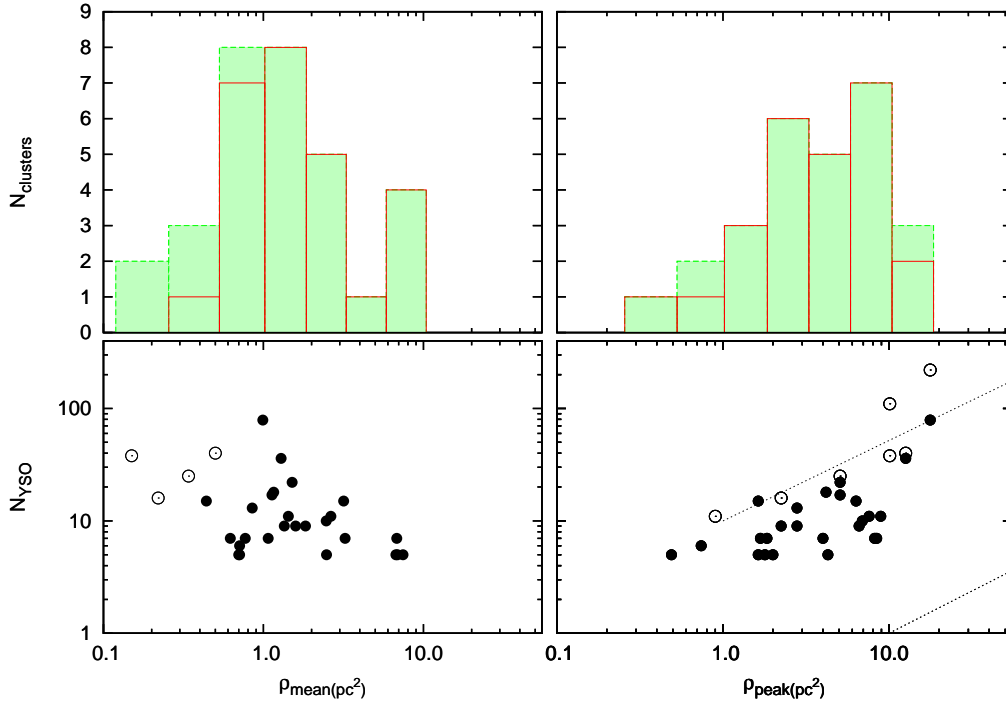


Figure 13. Histogram showing the mean YSOs surface density (upper left-hand panel) and plot of the mean YSOs surface density versus the number of cluster members (lower left-hand panel) for the sub-clusters and active regions. The symbols and histograms are the same as Fig. 12. Right-hand panels: Same as the left-hand, but for the peak YSOs surface density distribution. Dotted lines in the lower-right panel enclose all the regions with a slope of 0.8 as given in Chavarría et al. (2014).

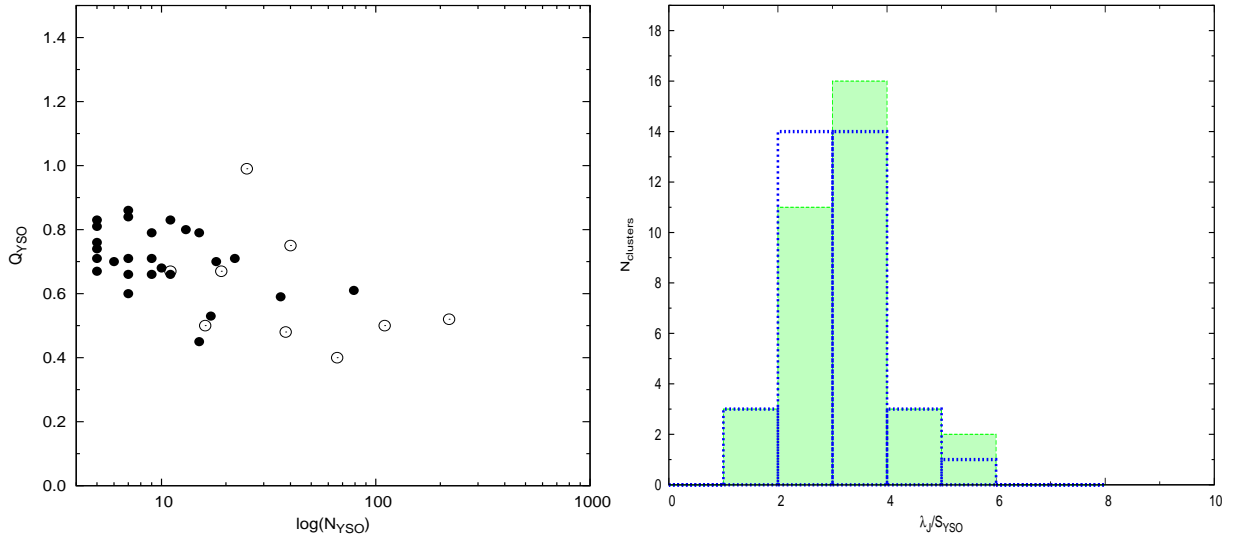


Figure 14. Left-hand panel: Structural Q parameters (Q_{YSO}) for the sub-clusters and active regions. The symbols are the same as Fig. 12. Right-hand panel: Histogram showing the distribution of the ratio between the cluster Jeans length (λ_J) and the mean projected distance between the members of sub-clusters and active regions.

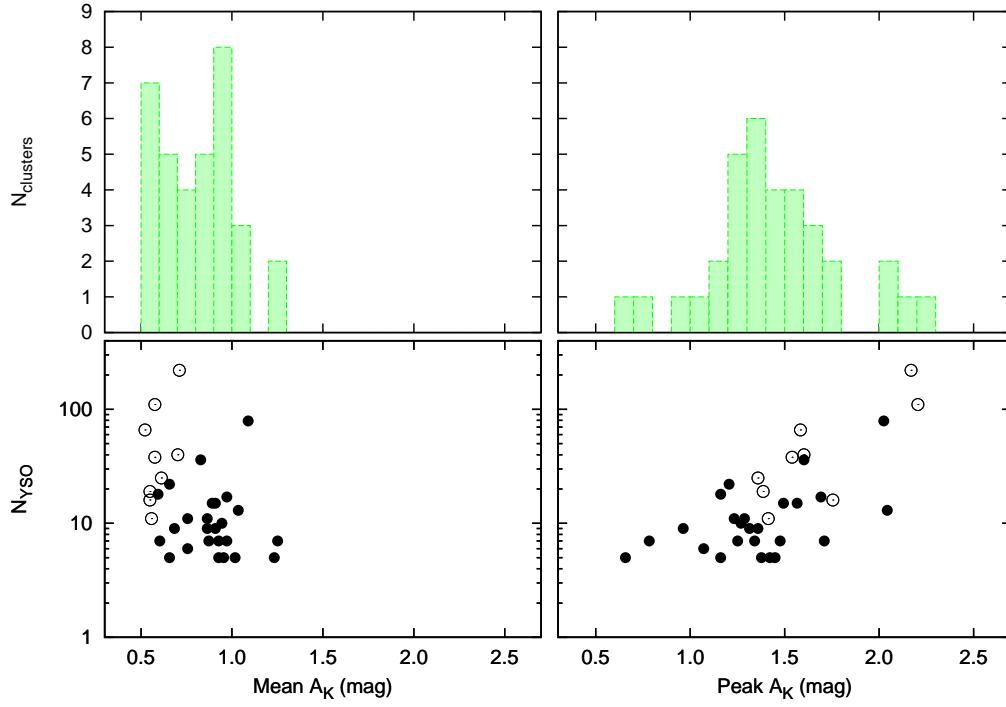


Figure 15. Histogram showing the mean K -band extinction (upper-left panel) and plot of the mean K -band extinction versus the number of cluster members (lower-left panel). The symbols are the same as Fig. 12. Right-hand panels: Same as left-hand, but for the peak K -band extinction distribution.

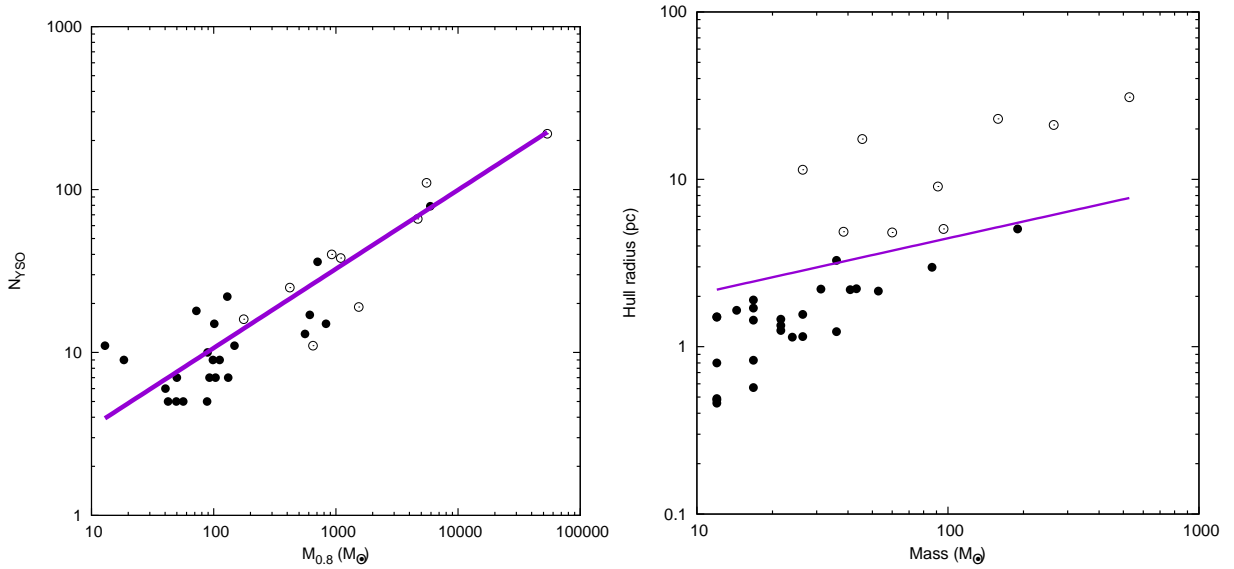


Figure 16. Left-hand panel: Relation between the number of YSOs ' N_{YSO} ' and the molecular mass above $A_K = 0.8$ mag ($M_{0.8}$) in the sub-clusters and the active regions. The number of YSOs is linearly correlated with the cloud mass with Spearman's correlation coefficient $r=0.8$ with 95% confidence interval of 0.6 to 0.9. Right-hand panel: Mass of the sub-clusters and the active regions are linearly correlated (Spearman's correlation coefficient, $r = 0.8$ with 95% confidence interval of 0.6 to 0.9) with the radius of the sub-clusters and the active regions. The solid line in right panel represents r_{lim} as a function of the mass (see text). The symbols are the same as Fig. 12.

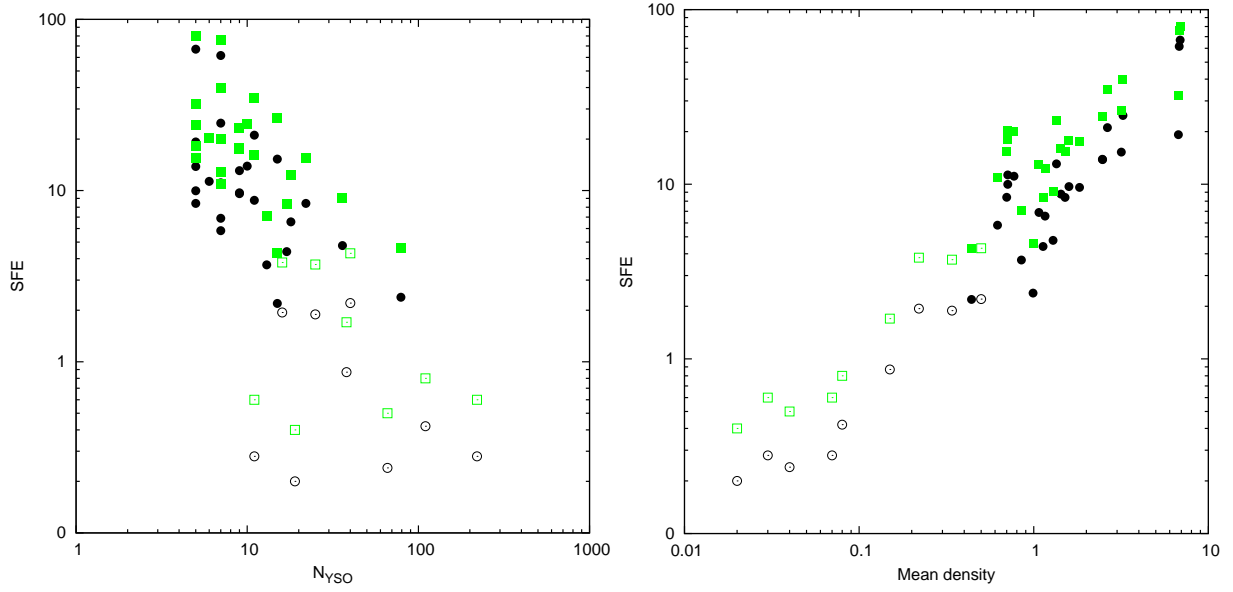


Figure 17. Star formation efficiency (SFE) (for Class I and Class II YSOs) in the sub-clusters and in the active regions with respect to the number of YSOs (left-hand panel) and the mean density (right-hand panel). The symbols are the same as Fig. 12. The filled and open squares represent SFEs with the assumed contribution of Class III sources in the sub-clusters and in the active regions, respectively.

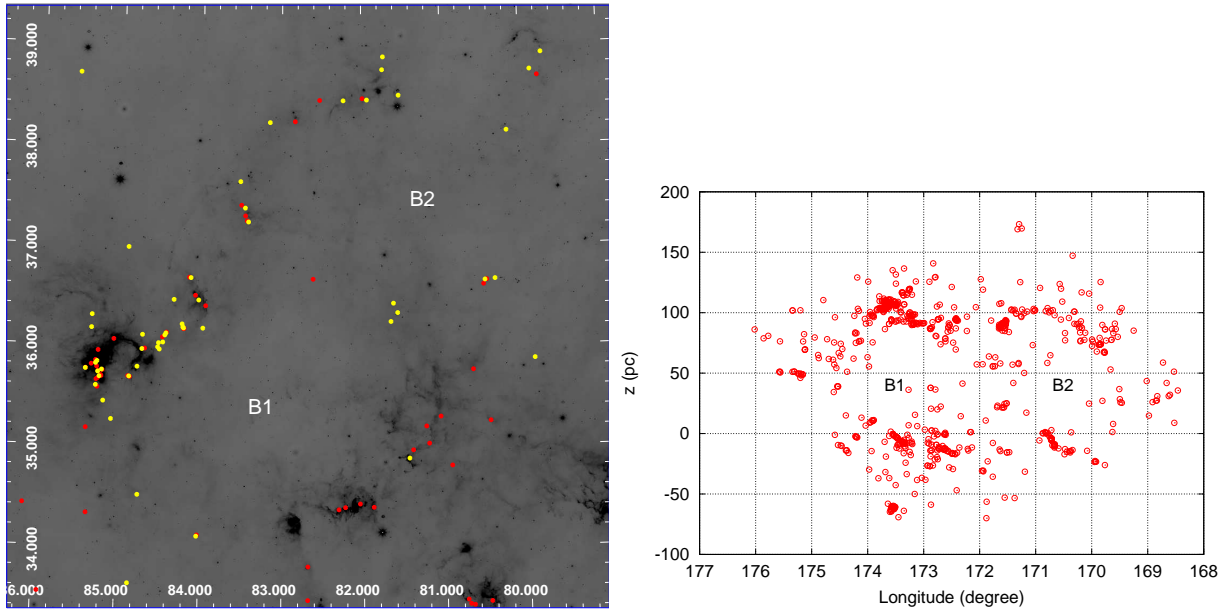


Figure 18. Left-hand panel: Spatial distribution of the YSOs having age < 1.0 Myr superimposed on the $6^\circ \times 6^\circ$ *WISE* $12 \mu\text{m}$ image of the Auriga Bubble region. The X-axis and Y-axis represent RA and DEC at the J2000 epoch. Right-hand panel: Distribution of all the identified YSOs in the $l-z$ plane.